

**Porosity, cracks, and mechanical properties of additively manufactured tooling alloys: a review**

BIDARE, Prveen <<http://orcid.org/0000-0003-2852-3498>>, JIMÉNEZ, Amaia, HASSANIN, Hany and ESSA, Khamis

Available from Sheffield Hallam University Research Archive (SHURA) at:

<https://shura.shu.ac.uk/33286/>

---

This document is the Published Version [VoR]

**Citation:**

BIDARE, Prveen, JIMÉNEZ, Amaia, HASSANIN, Hany and ESSA, Khamis (2022). Porosity, cracks, and mechanical properties of additively manufactured tooling alloys: a review. *Advances in Manufacturing*, 10 (2), 175-204. [Article]

---

**Copyright and re-use policy**

See <http://shura.shu.ac.uk/information.html>



# Porosity, cracks, and mechanical properties of additively manufactured tooling alloys: a review

Prveen Bidare<sup>1</sup> · Amaia Jiménez<sup>1,2</sup> · Hany Hassanin<sup>3</sup> · Khamis Essa<sup>1</sup>

Received: 29 December 2020 / Revised: 19 April 2021 / Accepted: 5 July 2021 / Published online: 16 September 2021  
© The Author(s) 2021

**Abstract** Additive manufacturing (AM) technologies are currently employed for the manufacturing of completely functional parts and have gained the attention of high-technology industries such as the aerospace, automotive, and biomedical fields. This is mainly due to their advantages in terms of low material waste and high productivity, particularly owing to the flexibility in the geometries that can be generated. In the tooling industry, specifically the manufacturing of dies and molds, AM technologies enable the generation of complex shapes, internal cooling channels, the repair of damaged dies and molds, and an improved performance of dies and molds employing multiple AM materials. In the present paper, a review of AM processes and materials applied in the tooling industry for the generation of dies and molds is addressed. AM technologies used for tooling applications and the characteristics of the materials employed in this industry are first presented. In addition, the most relevant state-of-the-art approaches are analyzed with respect to the process parameters and microstructural and mechanical properties in the processing of high-performance tooling materials used in AM processes. Concretely, studies on the AM of ferrous (maraging steels and H13 steel alloy) and non-

ferrous (stellite alloys and WC alloys) tooling alloys are also analyzed.

**Keywords** Additive manufacturing (AM) · Tooling alloys · Super alloys · Hybrid manufacturing · Post processing

## 1 Introduction

Recent advances in additive manufacturing (AM) technologies have enabled their use in many manufacturing applications. AM is becoming a useful alternative for the production of completely functional parts. This technology allows the production of parts with a complex and topologically optimized geometry with internal cavities that cannot be created with traditional manufacturing processes [1]. AM is currently applied in the most demanding industrial sectors, that is, the aerospace [2], energy [3], defense [4], and biomedical [5, 6] fields. Metal AM processes have enabled the repair of worn or damaged metallic parts. This capability is of special interest in the application areas for high-value components, for example, in tooling applications to repair damaged dies and molds [7]. Furthermore, the advantages provided by metal AM technologies can also be employed for the manufacturing of tooling applications (cutting tools, dies, and molds, among others) with enhanced geometries and material combinations. In mold-making applications, AM technologies allow the generation of cooling channels with a smooth curvature near the surface contour. Lattice structures can also be integrated into these channels. This enables efficient heat removal, which in turn increases the process productivity and lifetime of the tool [8, 9]. However, AM technologies still present certain issues, such as the variability of

---

✉ Prveen Bidare  
p.bidare@bham.ac.uk

✉ Khamis Essa  
K.E.A.Essa@bham.ac.uk

<sup>1</sup> School of Mechanical Engineering, University of Birmingham, Birmingham, UK

<sup>2</sup> TECNUN Escuela de Ingeniería, Universidad de Navarra, Manuel de Lardizábal 15, San Sebastián 20018, Spain

<sup>3</sup> School of Engineering, Technology, and Design, Canterbury Christ Church University, Canterbury CT1 1QU, UK

mechanical properties, microstructural characteristics, and surface roughness, which depend highly on the type of AM process and parameters selected. In addition, owing to the high cooling rates that occur during AM processes, residual stresses are generated that affect the in-service performance of the manufactured components. Given this context, this study focuses on the AM of tooling alloys.

This review paper addresses the AM of tooling alloys used in producing tools and dies for machining, forging, and metal forming processes. Considering these manufacturing processes, materials employed for tooling applications must have specific properties to ensure the quality of the generated parts and an acceptable tool lifespan. Depending on the application, tool materials should exhibit high resistance to wear, good thermal conductivity, high toughness, and impact strength, among other characteristics. The materials commonly employed in the tooling industry are tool steel, maraging steel, high-speed steel (HSS), non-ferrous metallic alloys, Co-Cr alloys, cemented carbides, ceramics, diamond, and aluminum alloys [10, 11].

During the last few years, the AM of metals has gained the attention of the tooling industry owing to its advantages in terms of material usage, the geometries that can be generated, and the design flexibility. When AM processes are employed to manufacture and repair various tools, they must ensure the characteristics mentioned above. These characteristics are closely related to the porosity, microstructural integrity, and residual stresses generated during the manufacturing, which are some of the most critical challenges in AM technologies [12–14]. Therefore, the selection of optimal process parameters that ensure the best mechanical and microstructural properties of the generated tools is of paramount importance.

In general, the AM of metals has been the focus of many recent research and review papers in the literature. However, until now, the microstructure and mechanical properties of metals created through AM have been analyzed with special emphasis on steel, aluminum, and titanium alloys only. This is due to the application of these alloys in demanding industries, such as the aerospace and automotive fields. Considering this, the present study aims to provide insight into the most relevant findings regarding the AM of tooling alloys employed for the manufacturing and/or repair of dies and molds. Special attention is paid to the specific characteristics required in the tooling industry, and the feasibility of AM technologies used to achieve these requirements is addressed.

The remainder of this paper is organized as follows. In Sect. 2, a review of metal AM processes will be presented with special emphasis on those that are most commonly used in tooling manufacturing applications, i.e., laser powder bed fusion, direct laser deposition, wire arc AM,

and metal binder jetting. The main characteristics of the materials employed for tool manufacturing are then reviewed. Sections 4 and 5 present a summary of the microstructural and mechanical properties of tools that must be ensured in the additive processes. Finally, some concluding remarks regarding the AM of tooling alloys are presented based on the research review described in the previous sections.

## 2 Metal AM processes

The development of metal AM processes has enabled the generation of completely functional and end-use metallic parts. Metal AM technologies can be divided into four different groups: powder bed fusion (PBF), directed energy deposition (DED), binder jetting (BJ), and material extrusion (ME) [15, 16]. Figure 1 shows a schematic diagram of the AM technologies discussed.

- (i) PBF. The energy source (laser or electron beam) delivers energy to a certain region of the powder bed to selectively fuse or melt the metallic powder. Once the entire section is melted, the powder bed drops, and additional powder is raked into the work area. The melting process is then repeated to create a three-dimensional component layer by layer. Laser powder bed fusion (L-PBF) and electron beam melting (EBM) are the most well-known technologies within this group [13, 17].
- (ii) DED. In this technology, a laser is employed as a heat source to melt the material in a powder or wire form and deposit it on a preheated surface using a nozzle. The material is deposited in the form of droplets to generate components layer-by-layer following a predefined path. Laser engineering net shaping (LENS), direct laser deposition (DLD), and wire-arc additive manufacturing (WAAM) technologies are the most important technologies in this group [17, 18]. Depending on the power source, WAAM technology can be divided into gas metal additive welding (GMAW), gas tungsten arc welding (GTAW), and plasma arc welding (PAW).
- (iii) BJ. In this technology, a binder agent is deposited on a powder bed to selectively glue the material. The part is created layer-by-layer by gluing the particles together. This binder agent must be removed later through sintering [17].
- (iv) ME. The material is selectively pushed through a heated nozzle or orifice to build parts in a layer-by-layer manner [17].

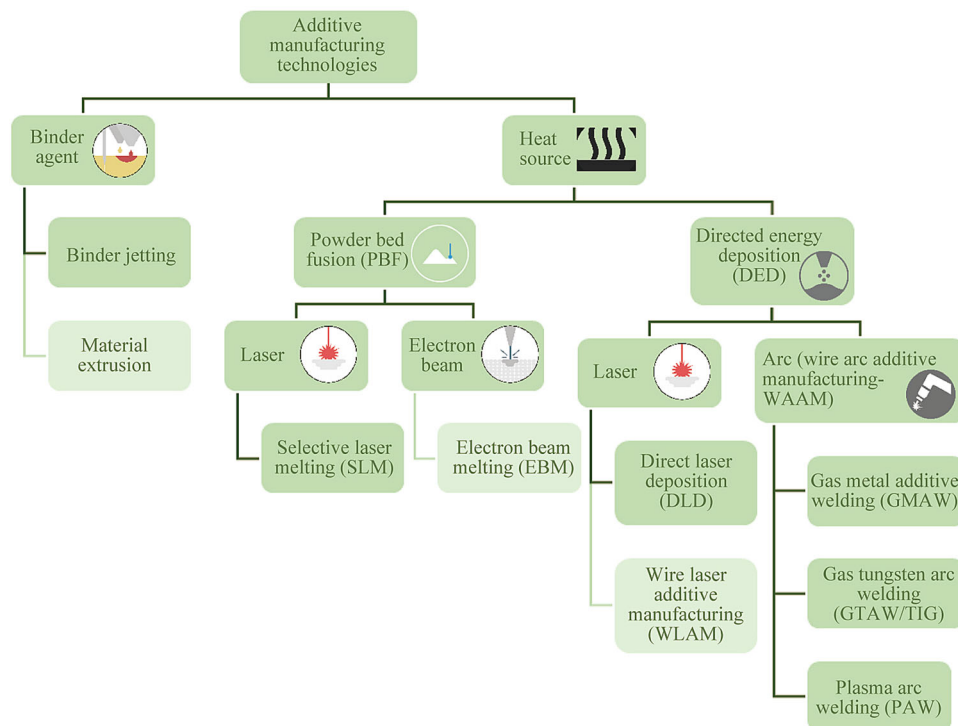


**Fig. 1** Schematic diagram of AM technologies

Among the metal AM technologies presented in this section, this paper focuses on those commonly employed in the manufacturing of tooling alloys (highlighted in Fig. 1), i.e., laser powder bed fusion, directed energy deposition, wire-arc additive manufacturing, and BJ. In the following sections, a further description of these technologies is presented, and the advantages, shortcomings, and challenges of each are discussed.

**2.1 Laser powder bed fusion (L-PBF)**

As mentioned above, powder bed fusion technology can employ a laser or electron beam as an energy source for melting the powder material. However, in this study, only L-PBF is considered as the most commonly employed technology. It is currently being used to manufacture high-value parts in high-tech industries. It employs a high-power density laser to selectively melt localized areas of the powder layer to create three-dimensional parts. When the particles are melted, a viscous flow from the surface tension joins them, generating a melt pool. The energy in the melt pool is then transferred to the surrounding powder through conduction, radiation, and convection [19]. After the consolidation of one layer, the powder bed is lowered, and a new powder layer is spread on the surface of the formerly created layer, that is, successive layers of powder are formed, and the process continues until completion of the fully dense 3D component according to the digital design [20–22]. Figure 2 shows a schematic of L-PBF technology [23].

The process parameters in L-PBF include the scan strategy, laser spot diameter, laser power, scan speed, scan line spacing, and the thickness of the powder layer. To obtain the best results regarding the porosity and mechanical properties of the generated part, these parameters must be optimized [21, 24–26]. Among these parameters, laser power has the most significant influence

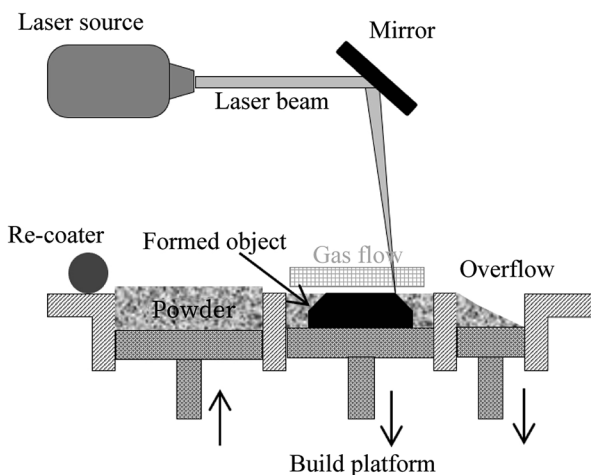


**Fig. 2** Graphical explanation of the L-PBF process [23]

on the porosity of the manufactured part [14, 27]. The characteristics of the powder (such as chemical composition, size, distribution, and shape) also have an essential effect on the component quality and properties. In addition, the gas flow direction and rate of the enclosed chamber must also be optimized to obtain the best results [28]. In fact, part delamination can occur if the gas flow is not adequately established. Furthermore, the height of the flow straightener from the powder bed and the type of shielding gas also affect the build quality [29]. Figure 3 shows some examples of applications created using L-PBF [30, 31].

Productivity is one of the most significant issues in L-PBF technology because of the time spent in laser scanning. Therefore, recent research and advancements in L-PBF have focused on improved productivity. In this regard, the use of quad laser systems to improve the productivity and reduce residual stresses has been tested [32]. By contrast, in situ shelling has been introduced to scan only a thin shell of the part, followed by hot isostatic pressing to minimize the time spent in laser scanning [33, 34]. Multi-laser systems are also being implemented to improve the productivity of the process. Meanwhile, additive industries have integrated powder handling/cleaning and post-processing of L-PBF components in the same multi-build chamber, which constitutes a chance for a series production [35]. Other studies have focused on improving gas flow systems to optimize consumption and process. Process monitoring has also been an object of research because it can help in increasing the understanding of the physics behind AM processes [36, 37]. The build plate temperature, ambient temperature, and pressure oxygen concentration, among other conditions, have a significant influence on the process behavior and the appearance of defects. Therefore, process monitoring is crucial. Recently, efforts have been made to develop advanced monitoring systems that enable the control of the laser power, position, melt-pool status, layer

distribution on the build surface, and temperature, among other influencing parameters [38, 39].

The L-PBF process offers advantages over other manufacturing processes. Complex geometries and parts with small features and internal cavities can be created using this technology. It enables the generation of topology-optimized parts and lattice structures with a reduced mass, which is particularly interesting for the aerospace industry. In addition, the produced parts have a high specific strength and stiffness.

However, the L-PBF technology also presents several limitations. Surface roughness is one of the major problems of this technology, and is caused by the layer-by-layer process, which leads to the widely known “staircase effect”. In addition to the process parameters, the powder size also affects the surface finish. When smaller particles are employed, and the layer thickness is reduced, a better surface finish can be obtained, but with the penalty of an increased production time [40]. In addition, parts created by L-PBF usually exhibit poor fatigue behavior owing to the residual stresses generated. These are the consequences of the thermal gradients that are created in the metallic part owing to the significant amount of heat generated during the manufacturing process [12].

L-PBF has other inherited issues, such as porosity and shrinkage of L-PBFed parts [24]. Shrinkage occurs during the liquid-to-solid transformation of the material, which is also responsible for accumulating residual stresses that deteriorate the performance of the part. Concerning the porosity and instability of the melt pool [41], a lack of fusion between powder particles [42], a narrow particle size distribution that reduces the packing density [43, 44], and scanning strategies are some of the factors that may promote the generation of low-density AM parts [12, 45]. Other issues include powder oxidation, which might occur owing to oxygen in the build chamber during the printing process [46]. These issues lead to a lack of confidence in

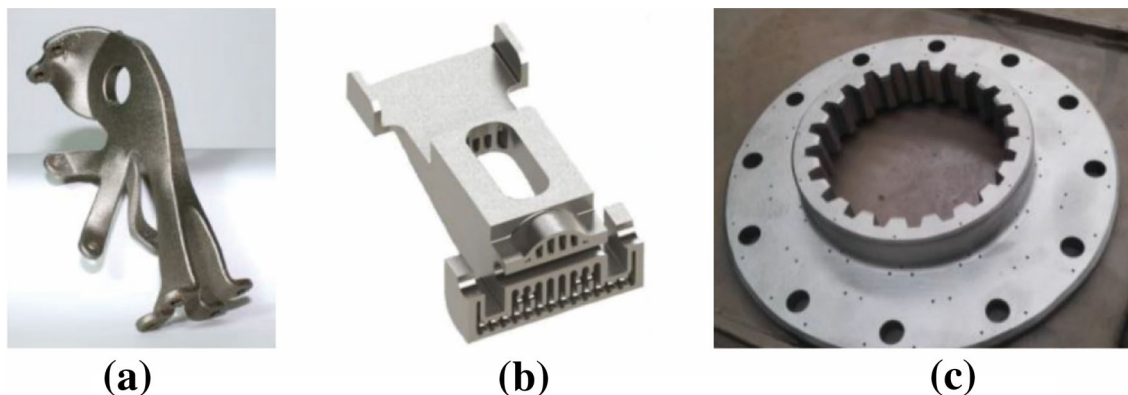


**Fig. 3** Applications created by L-PBF technology **a** topology optimised bracket for aerospace industry [30], **b** stopper and **(c)** connecting plate for automotive industry [31] (The figures are reused under the Creative Commons Attribution License.)

the quality obtained through L-PBF and need to be overcome in order for the technology to be fully applied in the production industry. In this context, it is important to understand the physics of the process to control the final results. As noted by King et al. [47] in their review paper, computer models can help in understanding the physics of the process, such as the interaction between the powder and laser. These models will enable the optimization of process parameters depending on the materials employed and the design geometries.

## 2.2 Direct laser deposition

Direct laser deposition (DLD) employs a laser as a heat source to melt the material and deposit it through a nozzle on the work surface. According to Thompson et al. [48], DLD is a direct deposition method that utilizes a metal wire and/or powder deposited on a building platform accompanied by simultaneous irradiation of a laser beam. Part of the heat provided by the laser is absorbed by the substrate on which the material is deposited, creating a controlled melt pool on the surface. The material is then delivered to the melt pool through a nozzle [49]. In addition, to minimize the risk of metal oxidation, an inert gas is usually delivered to the deposition area. This process is illustrated in Fig. 4 [50].

The DLD can be attached to a robot arm or integrated into a machine such that the nozzle follows a specific path to generate the desired geometry in a layer-by-layer manner. DLD is commonly employed for coatings and for repair of worn or damaged components, increasing interest in the automotive and aerospace industries owing to its cost savings.

As in other powder-based technologies, powder characteristics significantly influence the quality and properties of DLD manufactured parts. The chemical composition of the powder, particle size, distribution, morphology, and

laser parameters (laser power, powder feed rate, and scanning speed) must be optimized to obtain the desired physical and mechanical properties [51]. Another critical parameter in the DLD processes is the hatch or scanning pattern that defines the powder deposition path. The microstructure and mechanical properties of DLD parts can be controlled by changing the hatching pattern [52]. In addition, the nozzle inclination angle and the focus of the laser beam are essential factors that influence the properties of the printed parts. Figure 5 shows examples of industrial applications of the DLD process [53].

DLD enables the manufacturing of metal parts with higher productivity (higher building rates) compared to L-PBF technology [54]. In addition, through the DLD process, parts can be created from scratch, or the material can be deposited over specific regions of existing components and uneven surfaces to create a specific geometry or repair a broken feature. This characteristic of the process offers enormous flexibility in the manufacturing of metal components. Furthermore, in DLD processes, different powder materials can be used simultaneously, enabling the creation of functionally graded materials or customized alloys. Another advantage of the DLD technique is the low heat input required in the process (laser powers within the range of 1–5 kW), which reduces the distortion of the printed part and damages the building substrate [55].

However, some disadvantages and limitations must be considered when using a DLD. Dimensional inaccuracies, a rough surface finish, the so-called “staircase effect” part porosity, and residual stresses that lead to poor mechanical and fatigue behavior of the components are common issues to additive technologies in general and are the most typical limitations of this process. In addition, the DLD also presents particular issues, such as the oxidation of powder that may occur during the process. DLD systems are not usually integrated into a closed chamber in a controlled environment. Therefore, DLD systems usually deliver inert gas to

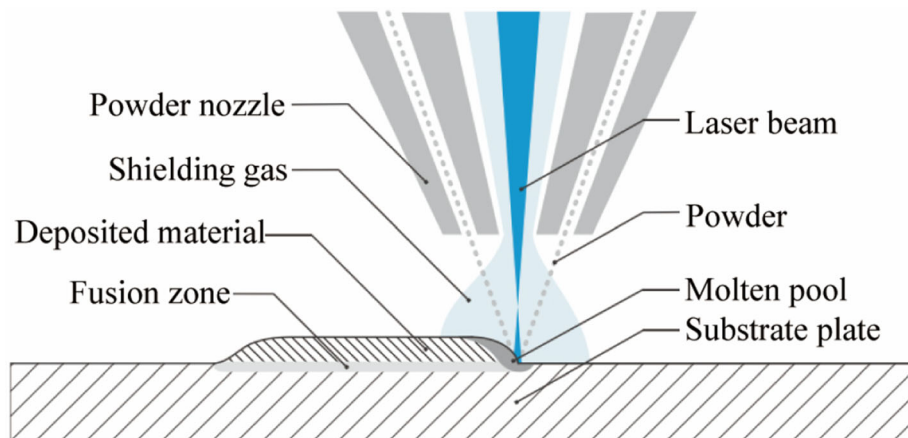


**Fig. 4** Schematic diagram of powder-based DLD process

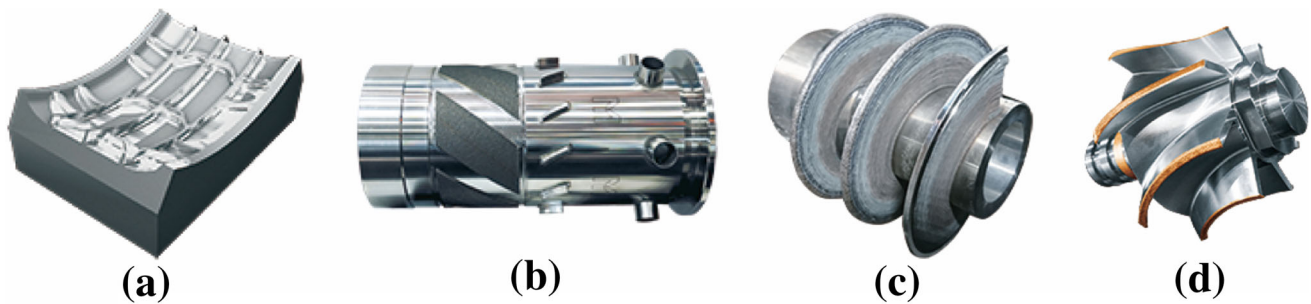


**Fig. 5** Industrial applications of the DLD process in Mazak Integrex i-400AM system (a) a mould insert, (b-c) general machinery and (d) surface coating added to an impeller [53]

the melt pool to limit the oxidation of the powder, as shown in Fig. 4. However, depending on the environment and the processed material, this might be insufficient to ensure the absence of oxides in the deposition, which may damage the integrity of the part. Furthermore, in comparison with PBF techniques, DLD samples show a lower hardness, higher ductility, and higher toughness [56].

Considering the limitations of DLD, as mentioned for the L-PBF process, computer models that can help in understanding the process and optimize the process parameters are of significant interest. As an example of the ongoing efforts to develop DLD models, Liu et al. [57] recently proposed a model for the evolution of the grain structure in the DLD process considering the influence of laser power and scanning speed parameters.

### 2.3 WAAM

WAAM is another remarkable technology that belongs to directed energy deposition AM technologies. It employs an electric arc as a heat source and a metallic wire as feed-stock to build components in a layer-by-layer manner. To 3D print components using WAAM, the nozzle movement can be provided by a robotic system or a numerically controlled machine table. WAAM systems can be created using commercially available components, i.e., a robotic system or numerically controlled table, a welding power source, a welding torch, and a wire feed system [58]. In addition, to avoid or decrease the oxidation issues during deposition, WAAM systems are usually enclosed in a chamber to provide an inert gas environment (similar to PBF systems), or they are equipped with local shielding gas mechanisms that deliver the inert gas. This last option increases the working space and allows the manufacturing of large metallic structures [59]. Figure 6 shows a schematic of the proposed WAAM technique [60].

The most remarkable advantage of WAAM technology is that it enables the generation of components with high deposition rates, reducing the fabrication time by 40%–60% compared with traditional subtractive manufacturing

processes [59]. Regarding other AM processes, the increase in the deposition rate allowed by the WAAM technology is also noticeable. For example, whereas L-PBF and DLD technologies achieve deposition rates of 0.1 kg/h and 1 kg/h, respectively, with WAAM systems, deposition rates of up to 5–6 kg/h can be achieved [61].

However, WAAM processes present disadvantages. In comparison to other AM technologies such as L-PBF, WAAM does not allow creating small details with such good resolution [58] and it generates parts with an inferior accuracy, mainly owing to the “stair-stepping” effect and higher surface roughness than other AM techniques [62, 63]. Figure 7 shows examples of geometries generated through WAAM technology [64–66].

In addition, residual stresses, which are a general issue shared by all AM technologies, are of particular importance in WAAM [58, 61]. Furthermore, WAAM technology also presents defects such as porosity, cracking, and deformations caused by residual stresses, which are also common in other AM processes.

To avoid or decrease the impact of the above-mentioned problems, there are several techniques, such as post-process heat treatment, interpass cold rolling, interpass cooling, peening and ultrasonic impact treatment, that have recently been applied to WAAM components and have shown beneficial effects on the residual stress fields, porosity, mechanical properties, and microstructural characteristics of WAAM parts [59, 62].

As in other cases, the process parameters have a significant influence on the final result obtained with WAAM. The travel speed, wire feed rate, current, and argon flow rate are some of the most critical parameters that must be controlled to obtain optimal results. Deposition patterns and deposition sequences must also be considered to obtain the best results [63].

### 2.4 Metal BJ

BJ is an AM technology in which a binder agent is deposited on a powder bed to selectively glue the powder

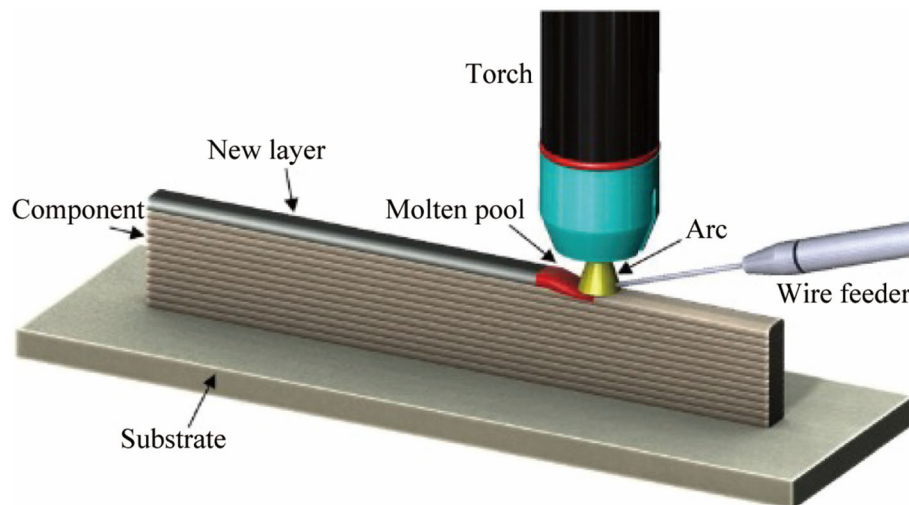


**Fig. 6** Schematic diagram of WAAM process [60] (The figure is reused under the Creative Commons Creative Commons CC-BY license.)

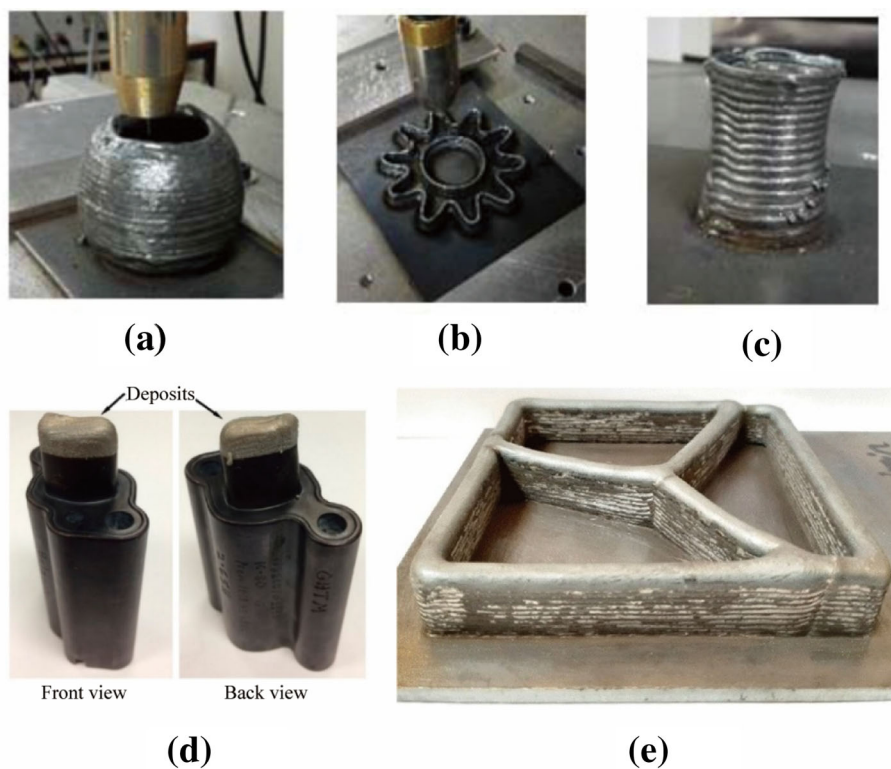


**Fig. 7** Various metal AM components produced by WAAM [64–66] (The figures are reused under the Creative Commons Attribution License.)

particles following a certain two-dimensional pattern. Once the layer is printed and cured, a new layer of powder is deposited in the powder bed on top of the previous layer, typically using a counter-rotating roller, and the binder agent is again delivered to create the part in a layer-by-layer manner [67–69]. Figure 8 shows a schematic of the BJ process [70].

The as-deposited part, which is usually called a green part, is fragile and requires further post-processing for strengthening purposes. To transform a green part into an end-use strength product through a post-processing, a series of operations must be conducted. Firstly, the green part must be separated from the unbound powder particles in the powder bed. To accomplish this, the powder bed is usually placed in a furnace. Special attention must be paid

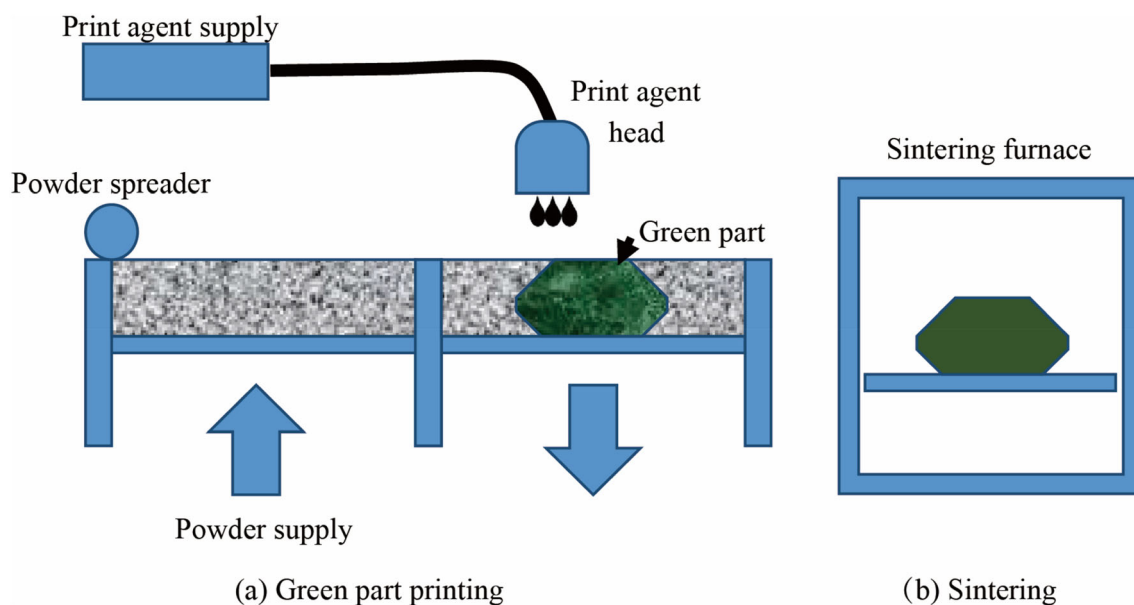


**Fig. 8** Layout of BJ process [70]

to ensure that the treatment does not alter or consolidate the unbound particles. The second stage is the debinding process, which consists of removing the binder agent. Finally, sintering must be applied to the part to densify and strengthen the green part by generating mechanical bonding between the particles [67].

The process parameters must be controlled and optimized to obtain the best results in the fabricated parts. For other AM processes, the powder particle size, distribution, and shape significantly influence the results. In addition, the binders employed, layer thickness, and post-processing also affect the quality of the generated part. All mentioned factors must be optimized to obtain the best results in terms of part density, surface roughness, accuracy, and mechanical properties, such as the strength and fatigue.

According to the materials employed in BJ, it theoretically allows the use of any material in powder form. Therefore, a wide range of ceramics, metals, biomaterials, and polymers have been used in this process. The use of these materials allows for the generation of parts for different applications. Figure 9 shows some examples of parts fabricated using BJ and different powder materials [71–73].

BJ has the advantage of being able to process, in theory, all materials in powder form. It enables the use of ceramic materials and metals with high reflectivity that are impossible or difficult to handle in laser-based AM technologies. The BJ process can generate parts with a relatively good surface quality. Depending on the powder characteristics and post-processing parameters, an average roughness of 5  $\mu\text{m}$  can be achieved. In addition, the generated components present isotropic properties, which can

be of particular interest in specific applications. Concerning the economy of the process, BJ requires lower energy consumption than other technologies and allows a high building rate, which improves the process productivity. Finally, it is worth noting that the amount of unused powder that can be recycled for successive processes is high. However, to reuse the powder, specific considerations must be considered. Any remaining binder agent must be completely removed. Furthermore, the presence of contaminants and changes in the size, morphology, chemical composition, and microstructure of the powder caused by the oxidation or sintering process must also be analyzed because such parameters may affect the quality of the successive powder bed printing processes.

The BJ technology also has certain shortcomings. It is a relatively new technology that requires further research to fully understand how process parameters may affect the final results. To obtain the best results, there is still a need to develop process models and simulations that can help in selecting the optimal process parameters for each desired design. Regarding the properties of the generated parts, although the mechanical properties are similar to those obtained through L-PBF processes, their fatigue behavior is more deficient owing to the relatively high porosity of the BJ parts.

Table 1 shows a comparative analysis of the main advantages and shortcomings of the AM techniques presented above.

### 3 Characteristics of tooling alloys

Considering their usual applications (stamping, forming, shearing, and cutting metals and forming plastics), tooling alloys must have resistance, toughness, and resistance to softening at high temperatures [74]. In the following sections, these properties will be further analyzed along with other desirable tool material characteristics.

#### 3.1 Machinability

Tooling materials are typically used for manufacturing molds and dies for casting and forging industries. They usually need finishing processes to achieve the tough tolerance requirements of these industries. Considering the need for machining to obtain the desired surface qualities and dimensional accuracies, the machinability of tooling materials is an important issue to consider.

Although not an intrinsic property of materials, machinability is a reference for evaluating the interaction between the tool material and the workpiece material to be cut [75]. This can be understood as the ease or difficulty by which a given material can be machined [76]. Depending on the application, machinability can be defined as the achievable surface finish, tool wear generated, or power consumption in a machining operation. It is also related to other factors such as the type of machining operation, cutting parameters, cooling conditions, cutting tool geometry, mechanical properties, and microstructural characteristics of the material to be machined [76, 77]. Traditionally, machinability has been quantitatively measured based on different criteria such as the number of parts machined prior to tool failure, the maximum cutting speed

achievable, and torque and power requirements [75]. The “machinability index” and “machinability rating” are other parameters employed to measure the machinability of a material. Specifically, the machinability rating ( $R_M$ ) can be expressed as a ratio of the material removal rate between the workpiece material of interest and a reference workpiece material

$$R_M = \frac{\xi}{\xi_{\text{ref}}} \times 100\%, \quad (1)$$

where  $\xi$  is the material removal rate, and  $\xi_{\text{ref}}$  is the reference material removal rate. The machinability rating has also been defined in terms of the cutting speeds as [76]

$$R_M = \frac{(V_{cT})_{\text{mat}}}{(V_{cT})_{\text{ref}}} \times 100\%, \quad (2)$$

where  $(V_{cT})_{\text{mat}}$  is the cutting speed at which the material of interest yields the defined tool life for a specific feed rate, depth of cut, tool material, and tool geometry.  $(V_{cT})_{\text{ref}}$  is the cutting speed at which the reference material with a machinability rating of 100% yields the defined tool life under the same conditions. In machining handbooks, machinability is usually related to the machining time needed to generate a predetermined flank wear value with a given cutting speed or on the power required to remove a unit volume of material during a turning operation. However, the machinability information provided by manufacturers and handbooks is not usually up-to-date. Such information is not entirely reliable because it does not consider differences in material grades or processes occurring during cutting, such as work hardening [78]. A vast amount of research is available in the literature focused on analyzing the machinability of different

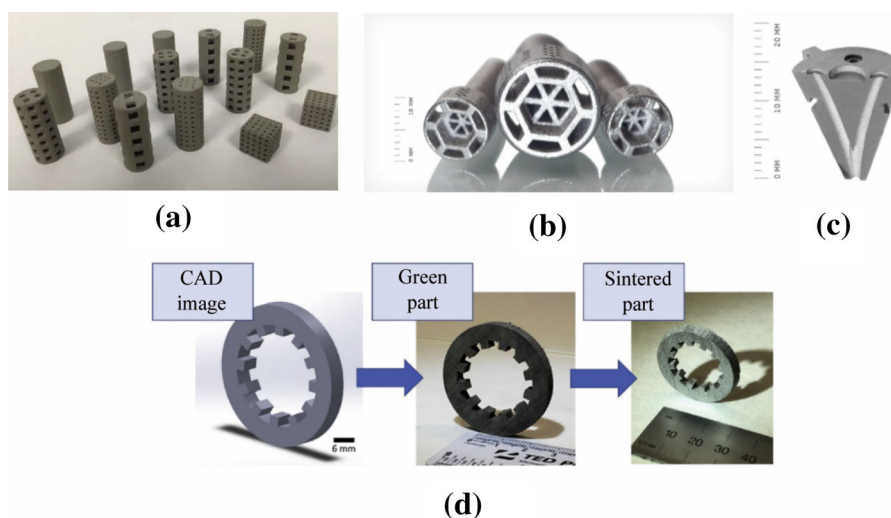


**Fig. 9** Examples of the different materials processed by BJ printing suited for various applications **a** compression samples for lattice designs [71], **b** hollowed components to save weight, **c** internal channels for efficient cooling [72] and **d** magnetic part [73]

**Table 1** Comparison of the four AM techniques mostly employed with tooling alloys

Technology	Advantages	Disadvantages
L-PBF	<ul style="list-style-type: none"> <li>(i) Complex geometries and parts with small features and internal cavities are possible to create</li> <li>(ii) It enables the generation of topology-optimised parts and lattice structures with reduced mass</li> <li>(iii) The produced parts have high specific strength and stiffness</li> </ul>	<ul style="list-style-type: none"> <li>(i) Surface roughness [40]</li> <li>(ii) Poor fatigue behaviour due to the residual stresses generated [12]</li> <li>(iii) Porosity and shrinkage of parts [24]</li> <li>(iv) Powder oxidation due to the presence of oxygen in the build chamber during printing [46]</li> <li>(v) Part delamination can occur if gas flow is not properly established.</li> </ul>
DLD	<ul style="list-style-type: none"> <li>(i) Enables manufacturing of metal parts with higher productivity</li> <li>(ii) Material can be deposited over specific regions of existing components and uneven surfaces to create a specific geometry or repair a broken feature</li> <li>(iii) Enormous flexibility</li> <li>(iv) It enables the creation of functionally graded materials or customised alloys</li> <li>(v) Low heat input needed, which reduces the distortion of the printed part and damage of the building substrate [55]</li> <li>(vi) Higher ductility and toughness than L-PBF [56]</li> </ul>	<ul style="list-style-type: none"> <li>(i) Dimensional inaccuracies, rough surface finish</li> <li>(ii) Part porosity and residual stresses that lead to poor mechanical and fatigue behaviour</li> <li>(iii) Powder oxidation</li> <li>(iv) Lower hardness than L-PBF [56]</li> </ul>
WAAM	<ul style="list-style-type: none"> <li>(i) High deposition rates [59]</li> </ul>	<ul style="list-style-type: none"> <li>(i) It does not allow to create small details with such good resolution [58]</li> <li>(ii) Generates parts with inferior accuracy and higher surface roughness [62, 63]</li> <li>(iii) Accumulation of residual stresses [58, 61]</li> </ul>
Metal BJ	<ul style="list-style-type: none"> <li>(i) Able to process all materials in powder form</li> <li>(ii) Relatively good surface quality</li> <li>(iii) Parts with isotropic properties</li> <li>(iv) Lower energy consumption than other technologies</li> <li>(v) High building rate</li> </ul>	<ul style="list-style-type: none"> <li>(i) The as-deposited part, is fragile and needs further post-processing for strengthening</li> <li>(ii) A relatively new technology that still needs more research</li> <li>(iii) Need to develop process models and simulations to optimize process parameters</li> <li>(iv) Poorer fatigue behaviour than L-PBF parts</li> </ul>

materials and alloys. Many studies [79, 80] have conducted an experimental tests of the material machinability based on different measurements, such as the cutting forces, surface roughness generated by a specific cutting pressure, tool wear, and cutting temperature. It is generally agreed that a specific parameter combination ensures optimal results in terms of surface quality, tool life, and power consumption.

For the machinability of tooling materials, Co-Cr-Mo-based alloys, also known as Stellite, are included in the group of difficult-to-cut materials. Stellites are designed to produce hard and thick coatings, and their use is recommended for forging die mold coatings owing to a high resistance to abrasive wear and toughness [81]. However, cobalt-based alloys also have high hardness, a dense but non-homogeneous structure, and low thermal conductivity, which lead to poor machinability [82]. Tool steels are another group of materials addressed in this study.

Machinability is influenced by many factors, such as the chemical composition, inclusions, and thermo-mechanical properties [83]. The machinability of martensitic hot worked steel is mainly influenced by the amount of non-metallic inclusions, such as manganese sulfides, and the hardness of the steel.

Regarding the machinability of additively manufactured tooling components, studies have focused on analyzing the machinability of components in which a coating layer has been additively deposited [84, 85]. When high surface quality and precision are required, the additively deposited coating layers require post-processing machining operations [85]. In some cases, the properties that make these materials suitable for harsh environments are also responsible for their low machinability. Different process parameters were monitored during machining to analyze the machinability of these materials. Cutting forces, specific cutting pressure, cutting temperature, surface

finish, power consumption, and residual stresses, among other factors, have been employed as machinability criteria, and the influence of the cutting parameters on their values has been studied to find optimal parameters that ensure the best results [80, 81, 84–86].

### 3.2 Reparability

During their life, tool materials are subjected to thermal and mechanical loads, impacts, and harsh environments, which may lead to erosion, wear, damage to their surface quality, or even cracking [87]. To avoid the high economic cost of a total tool replacement, dies, molds, and general tools are usually repaired.

To repair damage molds and dies, arc welding, cold-spray, and electro-spark techniques have been used. In recent years, laser-based and electron beam-based additive manufacturing techniques have gained attention as alternative repair options [88]. Among the different material deposition techniques, fusion welding has proved to be the optimum method for repairing molds and dies [88, 89]. The repair procedure usually consists of excavation to remove the damage and debris, followed by a clean-up of the surface and subsequent deposition of the filling material. Usually, a final machining step is required to generate the original surface shape. Regarding the repair techniques, options for material deposition during die and mold repair. Figure 10 presents the summary of the most employed approaches.

Once the deposition process is selected, the appropriate filling materials must be chosen when considering both the chemical composition of the substrate and the filling materials to ensure appropriate matching and good weldability. The final results of the repair depend not only on the materials engaged, but also on the welding parameters employed, which influence the microstructure and behavior of the welding and, in turn, those of the repaired tool.

### 3.3 High wear resistance

Wear resistance is the ability of tooling materials to withstand unfavorable working conditions without wear. For example, in the machining industry, tool wear control is crucial and might lead to the generation of out-of-

tolerance surfaces and/or defects in generated components, which leads to time and economic costs. Therefore, extensive research has been conducted to analyze the suitability of different tool materials, coating materials, and cutting conditions that can improve the wear resistance of the tool. Cemented carbides and high-speed steels are the most common materials employed for cutting tools, accounting for 53% and 20% of the market, respectively.

Recent research on the wear resistance of tooling alloys has focused on different alternatives to improve the wear behavior of these materials. Ahn et al. [90] developed a technology to improve the wear resistance of hot forging dies by the deposition of Stellite material through DED technology. Hot forging experiments were conducted to compare the wear resistance and quality of the products obtained with a designed die and a conventional die. It was shown that the proposed technology can dramatically improve both the wear resistance and quality of the products in hot forging applications. Cora and Koç [91] analyzed the benefits provided by eight different coatings applied to a tool steel material employed in stamping processes concerning the wear resistance. Experimental wear tests were conducted in which the specific wear rate, microscopic examination, and 3D surface roughness were analyzed as the wear parameters. The authors observed that among the coating materials tested, TiAlN and CrN showed a slightly higher wear resistance.

### 3.4 Thermal conductivity

Thermal conductivity can be defined as the ability of a material to conduct heat [92]. It can also be defined as the rate at which heat is transferred by conduction through a unit cross-sectional area owing to a temperature gradient normal to it. The thermal conductivity of a material  $k$  can be extracted from Fourier's law of heat conduction as

$$k = \frac{\Delta Q}{\Delta t} \frac{1}{A} \frac{x}{\Delta T} = \frac{\Delta Q}{A \Delta t} \frac{x}{\Delta T}, \quad (3)$$

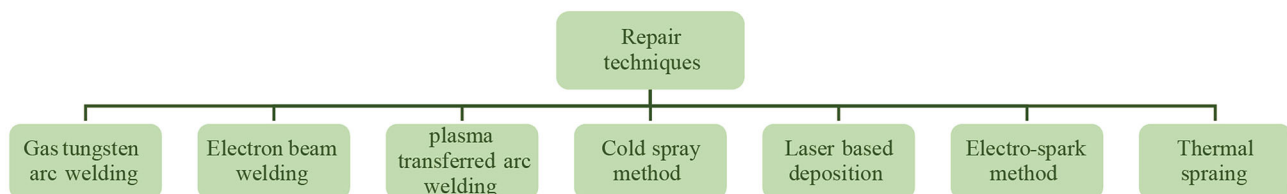


**Fig. 10** Options for material deposition during die and mold repair

where  $\Delta Q/\Delta t$  is the rate of heat flow,  $A$  the total cross-sectional area of the conducting surface,  $\Delta T$  the temperature difference, and  $x$  the thickness of the conducting surface separating the two temperatures.

Thermal conductivity is particularly important in the stamping/press hardening industry. Regarding the production cost, tooling is one of the main factors to consider because it can result in up to 20% of the cost of the final product [93]. This cost is associated with the design, manufacturing, and maintenance of the tool and its influence on the component cycle time and quality. This cycle time is highly affected by the cooling rate, which, in turn, depends on the thermal conductivity of the tool material. High-thermal-conductivity materials allow fast cooling rates and shorter cycle times. In addition, tool materials that allow high cooling rates also ensure a higher hardness of the produced components.

### 3.5 Toughness

Toughness is the ability of a material to withstand external forces without fracturing. Traditionally, it has been defined as the ability of a material to dissipate deformation energy without crack propagation. In terms of crack propagation, it can also be considered as the resistance of the microstructure against a “crack-driving force” [94].

Materials can be toughened by intrinsic mechanisms, as in the case of metals, in which the toughness is enhanced by changing the nature, distribution, and/or properties of second-phase particles to suppress damage through extrinsic toughening and extrinsic mechanisms, as in the case of ceramics. Ceramic materials are brittle and impossible to toughen intrinsically; therefore, microstructures must be used to promote the transformations required for toughening. Some tool steels have also been used to enhance their toughness. This is the case for AISI D2 cold-work tool steel, which exhibits a good behavior in terms of deformation, wear and corrosion resistance, and dimensional sensibility, but a low level of toughness [95]. Viale et al. [95] attempted to improve the toughness of AISI D2 steel by adapting the chemical composition of the material to reduce the volume fraction of primary chromium carbides that are responsible for the low toughness.

In addition to microstructural changes, heat treatments have also been tested to improve the toughness. For example, Cornacchia et al. [96] investigated the influence of aging on the microstructure and fracture toughness of die steels. They observed that, for the H13 steel commonly employed for dies, the aging treatment promoted fracture toughness.

### 3.6 Impact strength

The impact strength of a material is defined as its capability to resist a sudden applied load or force. It is normally conveyed as the amount of mechanical energy absorbed during deformation under the applied impact loading and is expressed as the energy lost per unit of thickness. The impact strength of tool materials is a crucial property for applications such as punches, rivets, and chisels [10]. The impact strength is related to the fatigue behavior of the components, which is of special importance in applications such as forging dies. In fact, most forging dies fail owing to the impact of fatigue cracks [97].

Lee and Chen [98] conducted an experimental investigation of the relationship between the mechanical properties and hardness of materials employed for cold-forging dies. According to the impact strength, they observed that the mechanical properties increased with an increase in the material hardness. Ebara and Kubota [99] conducted a failure analysis of hot forging dies for automotive components. They observed that impact failure led to a fracture in the component surface (concretely, a flange yoke die) after the forging process was repeated 2 000 times. Based on impact tests, the authors also noted that the impact fracture toughness depended on the testing temperature, and consequently, different fracture types were observed depending on this temperature.

### 3.7 Lubricating properties

The lubricant should ideally provide a continuous layer between the tool and workpiece to reduce friction and wear, prevent pickup on the workpiece, remove debris from the tool/workpiece interface, and extract the heat generated during the process away from the tool [10, 100]. Wilson [101] remarked that different lubrication regimes could be distinguished.

- (i) A thick film lubrication regime. The surface is separated by a continuous film of lubricant that is much thicker than the roughness of the surfaces involved. In this case, friction is governed by the properties of the lubricant. Wear is unlikely to occur, but it can appear as a consequence of corrosion.
- (ii) Thin-film lubrication regime. In this case, the lubricant thickness is between 3- and 10-times the RMS roughness of the surfaces, and the surface roughness can have a significant influence on the lubrication. However, as in most sections, the lubrication film is larger than the asperities of the surfaces, and the friction behavior is similar to that in the thick-film regime.

- (iii) Mixed lubrication regime. This occurs when the film thickness is much lower than 3-times the RMS value of the surface roughness. In this case, a significant fraction of the contact load between surfaces was carried by the asperities. Typically, lubricants contain compounds that react chemically with the surfaces and form a tightly adhered lubricant film that can prevent metal-to-metal contact, welding, and pick up at the asperity collisions.
- (iv) Finally, when all loads between the surfaces are carried by the asperities, the system is in the boundary lubrication regime, in which the friction is governed by the mechanics of the local deformation of the asperities and the physics and chemistry of the surfaces.

From the explanation above, it is evident that thick and thin-film lubrication regimes are the most desirable as they reduce friction and wear.

In machining operations, tool hardness decreases with an increase in the temperature in the cutting area. This leads to a faster development of wear mechanisms that, in turn, shorten the tool life. During these operations, cooling and lubrication are mainly intended to remove the heat from the cutting area and decrease the friction between the tool and the workpiece to avoid the fast development of wear mechanisms [102]. It has been shown that, with the use of lubrication, an 80% decrease in friction can be achieved. This enables machining to be conducted at high cutting speeds without decreasing the tool life.

In recent research, the use of self-lubricating materials has been analyzed to improve the friction and wear behavior of cutting tools during machining. Wu et al. [103] created a ceramic tool material in which a metal-coated solid lubricant powder was added. The self-lubricating tool showed notable improvements in the microstructure and mechanical properties, and better frictional behavior and wear resistance than the corresponding cutting tool during dry cutting experiments. Torres et al. [104] attempted to overcome the tribology problems appearing in the hot stamping of aluminum alloys by using iron-based and nickel-based self-lubricating laser claddings with the addition of solid lubricants. Self-lubricating claddings showed lower friction than tool steel. In addition, material transfer from the aluminum counter body was found to be low because of the higher resistance to adhesion wear and galling than the reference steel.

### 3.8 Additional coating compatibility

To reduce friction coefficients and in turn improve the tool life, surface finish, and power consumption, coatings are

usually applied to the tool materials [10]. To obtain the best results from the coatings, compatibility between the substrate and coating materials should first be ensured.

In the case of cutting tools, substrate materials are usually coated with different alloys, mainly TiC, TiN, TiCN, TiAlN, AlTiN, AlCrN, and Al<sub>2</sub>O<sub>3</sub>, to enhance their adhesive and abrasive wear resistance [105, 106].

Tool coatings are increasingly used in forming, die casting, and injection molding. H13 tool steel, commonly employed for the aforementioned applications, has been recently coated using AM technologies. Many authors have noted that the use of alloy powders with the same or similar chemical compositions to the substrate material ensures better metallurgical bonding, a smooth surface, and similar properties along with the interface [91, 107].

### 3.9 Heat-treatable

Finally, it has been shown that heat treatments enhance the mechanical properties of certain materials; therefore, they are also commonly applied to tooling materials. As for metal forming, the microstructure of most alloys in an as-cast condition is quite heterogeneous, and they must be homogenized at high temperatures to improve their workability [10].

Owing to the stringent requirements regarding tooling material properties, researchers have focused their attention on different alternatives to improve such properties. Different heat treatments have been tested in tooling materials to analyze their influence and possible benefits that can be added. Qamar [108] conducted an experimental test in which the H11 tool alloy, which was employed in metal forming applications, was subjected to different heat treatments, such as annealing, austenitization, air cooling, oil quenching, and single and double tempering. This study aimed to obtain the most suitable combination of treatments that led to the best results. Double tempering of oil-quenched samples was found to be the optimal heat treatment combination for obtaining hardness, toughness, and high yield strength, tensile strength, and ductility.

## 4 Microstructural and mechanical properties of tooling alloys

As concluded by Herzog et al. [109] and Gorsse et al. [110], among others, the high-temperature gradients that occur in AM processes have an influence on the grain microstructure generated and, consequently, on the mechanical properties of the built parts. Depending on the materials involved, different microstructural evolutions can occur. In addition, the anisotropic conductivity along the part is also responsible for the resulting anisotropic

microstructure, which in turn leads to anisotropic properties along the created components as well. Both reviews cited above show how the microstructural characteristics of AM steel, aluminum, titanium, and high-entropy alloy parts are correlated to the resultant component properties. In this section, microstructural features such as density, micro-hardness, and micro-cracking of AM parts fabricated from tool steels and non-ferrous tooling alloys are described. These characteristics are also correlated to the static and fatigue properties of the parts.

#### 4.1 Ferrous alloys

Steel alloys are the most relevant materials that comprise a group of ferrous alloys. In the most common applications, steel is required to provide a combination of corrosion resistance, strength, ductility, hardness, toughness, and wear resistance, along with low production prices and a variety of achievable microstructures and functionalities [8]. In the tool and die making industries, steel alloys with good yield strength, high hardness, and abrasion resistance are required.

##### 4.1.1 Properties of AM maraging steels

Maraging tool steels are steel alloys that exhibit superior strength and toughness while maintaining a good weldability and dimensional stability during aging. These properties make them especially suitable for high-performance aerospace and motor racing applications, such as rocket motor castings, drill chucks, punching tools, plastic injection molds, and metal casting dies. Among the steel alloys, carbon-free maraging steels, particularly 18Ni-300/1.2709, are currently the most widely employed in AM processing [8]. Compared with high-carbon tool steels that are also employed for these applications, the use of maraging steel corrosion and quench cracking can be avoided. This good performance is due to the lower carbon content and high nickel content and the absence of carbides in these alloys, as shown by Monkova et al. [111]. The authors studied the mechanical properties of untreated and heat-treated MS1 maraging steel. Samples were generated using L-PBF with different orientations. The authors observed that part orientation and heat treatment influenced the mechanical properties of the samples. During the tensile tests, the untreated samples suffered significant plastic deformation before breakage. The annealed samples exhibited a lower yield strength and higher ductility. In this case, the samples broke owing to a brittle fracture. In addition, concerning the cutting tool industry, it has been shown that the use of additively manufactured maraging tool inserts improves the removal of heat from the cutting

area. This in turn improves the cycle time and productivity of the cutting tools.

Jäggle et al. [112] conducted an experimental investigation in which L-PBF and DLD AM technologies were used to generate maraging samples, and their properties were compared with those of conventionally manufactured samples. In the DLD process, the laser power was set to 3 kW, whereas during the L-PBF process, a concept laser M3 linear machine was employed with a laser power of 100 W. The DLD samples showed higher hardness values than the conventional and as-deposited L-PBF samples. According to the authors, this was due to the heat treatment inherent in the DLD process. A heat source is continuously applied to the previously deposited layers when the adjacent or/and overlaying layers are melted. Because of this intrinsic heat treatment, early stage precipitation is induced, which leads with a higher hardness of the DLD samples when compared with the as-received wrought and as-deposited L-PBF samples. However, when a subsequent aging treatment was applied to the samples, the trend shown in Fig. 11 was observed.

As the aging treatment progresses, the DLD material softens, and after 10 min of treatment, the conventionally produced samples become harder.

Special attention is usually paid to controlling and improving the density of parts generated by AM technologies, as this property affects the mechanical and fatigue behavior of the parts. Many studies have shown that it is possible to create crack-free samples with relative densities above 99% by using AM [113–118]. In these studies, the generated density ( $\psi$ ) is usually related to the so-called energy density, which can be expressed in terms of other process parameters as [26]

$$\Psi = \frac{P}{vht}, \quad (4)$$

where  $P$  and  $v$  are the laser power and scan speed, respectively;  $h$  is the scan spacing; and  $t$  is the layer thickness.

Tan et al. [113] investigated the microstructure and mechanical properties of maraging 300 samples manufactured using L-PBF. They analyzed the influence of energy density on the resultant part properties and observed that for values below 35 J/mm<sup>3</sup>, porous parts were generated owing to the lack of fusion issues. In addition, as shown in Fig. 12, the porosity decreased with an increase in the laser energy. However, the highest values of energy density led to a decrease in the density of the parts. According to their investigation, an energy density of 67 J/mm<sup>3</sup> must be employed to obtain the optimal density (99%) of the manufactured part, and the  $P$ ,  $v$ , and  $h$  parameters in Eq. (1) must be set to 285 W, 960 mm/s and 110  $\mu$ m, respectively, for the best results.

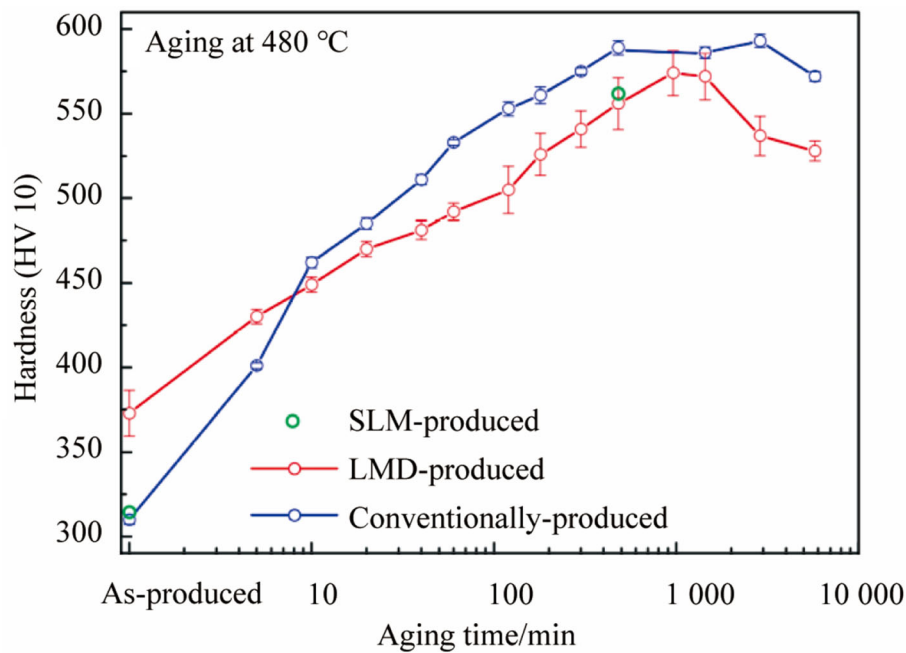


**Fig. 11** Microhardness of conventionally produced and DLD (or LMD)-produced material as a function of aging time at 480 °C. Additionally, the hardness of L-PBF-produced material in the as-produced state aging time at 480 °C (Additionally, the hardness of L-PBF-produced material in the as-produced state and after 480 min aging is shown [112]. The figure is reused under the Creative Commons Attribution License.)

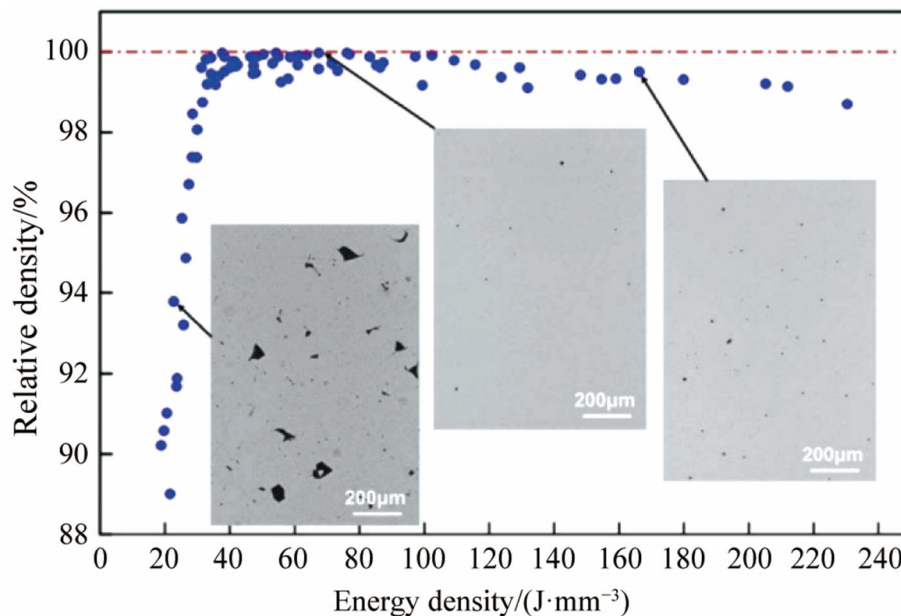


**Fig. 12** Effect of laser energy on the relative density of L-PBF parts [113] (The figure is reused under the Creative Commons CC BY license.)

Similarly, Bai et al. [114] investigated the influence of process parameters on the density of maraging steel 300 samples generated using L-PBF with a laser power of 200 W. They observed that the density increased with an increase in laser power up to a specific value and then decreased with the increase in laser power, scanning speed,

and scanning space. Another conclusion extracted from their work is that, if low laser power and high scanning speeds are employed, a low energy density is obtained (see Fig. 12) and the metal employed remains unmelted. By contrast, if higher laser power and a low scanning speed are employed, the energy density is sufficient to melt the metal

properly. However, in these cases, strong vaporization and spatter occur, leading to voids and inclusions in the samples. These same issues were also observed when small scanning spaces were employed. However, a high scanning space might leave unmelted powder and consequently a low relative density. Therefore, it can be concluded that all parameters must be optimized in each case to obtain the best results in terms of the relative density.

Becker and Dimitrov [115] employed the same maraging steel alloy to analyze the influence of the exposure strategy on the density of parts generated by L-PBF. In their tests, the layer thickness was set to 30  $\mu\text{m}$ . The authors remarked that the scanning strategy had a considerable effect on the part porosity obtained and, according to the results obtained in their study, a double exposure scanning strategy enabled the generation of parts with higher density. In addition, they observed that optimal results were obtained when a hatch spacing of 0.7 d and a laser speed of 600 mm/s were employed.

The influence of the process parameters on the generated part density was also studied by Kempen et al. [116]. Specifically, they studied the effect of layer thickness and scanning speed on the microstructure and mechanical properties of 18Ni 300 steel samples. L-PBF technology with a laser power of 100 W was employed for sample manufacturing. The authors observed that an increase in layer thickness and/or in the scanning speed led to a decrease in the density of the manufactured parts, which in turn implied a decrease in the macro-hardness (see Fig. 13). However, they noted that these parameters had no significant effect on the microhardness of the manufactured samples.

Yasa et al. [117] studied the effect of laser re-melting on the density of additively manufactured parts. Even when the samples with and without re-melting presented similar density values (above 99%) according to Archimedes' method (above 99%), optical micrographs taken from the generated samples showed differences between the samples. Figure 14 shows micrographs of the top and side cross-sections of the samples [117]. It can clearly be seen that those parts subjected to re-melting (parts 2 and 3 in Fig. 14) present less porosity than the sample manufactured without re-melting (part 1 in Fig. 14).

In addition to the good density values achieved, the authors observed that the microhardness of additively manufactured samples was even higher than that of conventionally manufactured parts.

Regarding the mechanical properties of maraging steels, it has been shown in the literature that additively manufactured maraging steels exhibit properties that are generally comparable with those of conventionally produced materials. Maraging steels that are processed through

L-PBF technology have shown a higher yield and ultimate tensile strength in a non-treated form [114–116, 118].

Kruth and Humbeeck [119] analyzed the influence of aging parameters on maraging 300 steel samples created by hybrid manufacturing combining L-PBF additive technology and re-melting. In their study, the authors observed that aging of the samples led to an increase in hardness and strength. Similarly, Tan et al. [120] studied the mechanical properties of the same alloy manufactured by L-PBF and aged at 490  $^{\circ}\text{C}$  for 6 h. The tests showed that owing to the strengthening of the precipitated phase, the hardness of the additively manufactured samples increased after heat treatment.

As shown above, most studies in the literature regarding AM of maraging steels are focused on L-PBF technology. However, few studies have analyzed the results obtained using DLD. As an example, low-carbon maraging 1.2709 steel is commonly employed for the manufacturing of injection molds through DLD technology. Junker et al. [121] analyzed the effect of selected DLD parameters on the mechanical properties of 1.2709 samples. They observed that a higher laser power generally led to a more homogeneous hardness distribution in the samples, that is, a more homogeneous inner structure. Nevertheless, when compared with conventionally created parts, the DLD parts have a lower hardness.

#### 4.1.2 Properties of AM H13

H13 alloy is a chromium-based tool steel usually employed in the manufacturing of die casting, forging dies, pressure casting dies for the automotive industry, and injection molds owing to the combination of high hardness, wear resistance, toughness, and resistance to high operating temperatures [122–124]. These tools have been traditionally manufactured from large blocks of materials, which are costly and time-consuming. Recently, the feasibility of AM for the manufacture of dies has been tested. In the die casting and forging die industry, DLD technology is the most commonly used.

Owing to its wide application, many studies have focused on the AM of H13. The most relevant conclusions extracted from studies that analyze the microstructural and mechanical characteristics of H13 manufactured through L-PBF are first presented below.

In their work, Yan et al. [125] noted that, in addition to the formation of a martensite structure in L-PBF of H13, a partial decomposition of the material into fine  $\alpha\text{-Fe}$  and  $\text{Fe}_3\text{C}$  precipitates along with the retained austenite occurred. From a TEM analysis, the authors observed that the lattice of the resulting  $\alpha\text{-Fe}$  phase was slightly distorted owing to the enhanced Cr, Mo, and V contents. According to the mechanical properties of the samples, they noted that

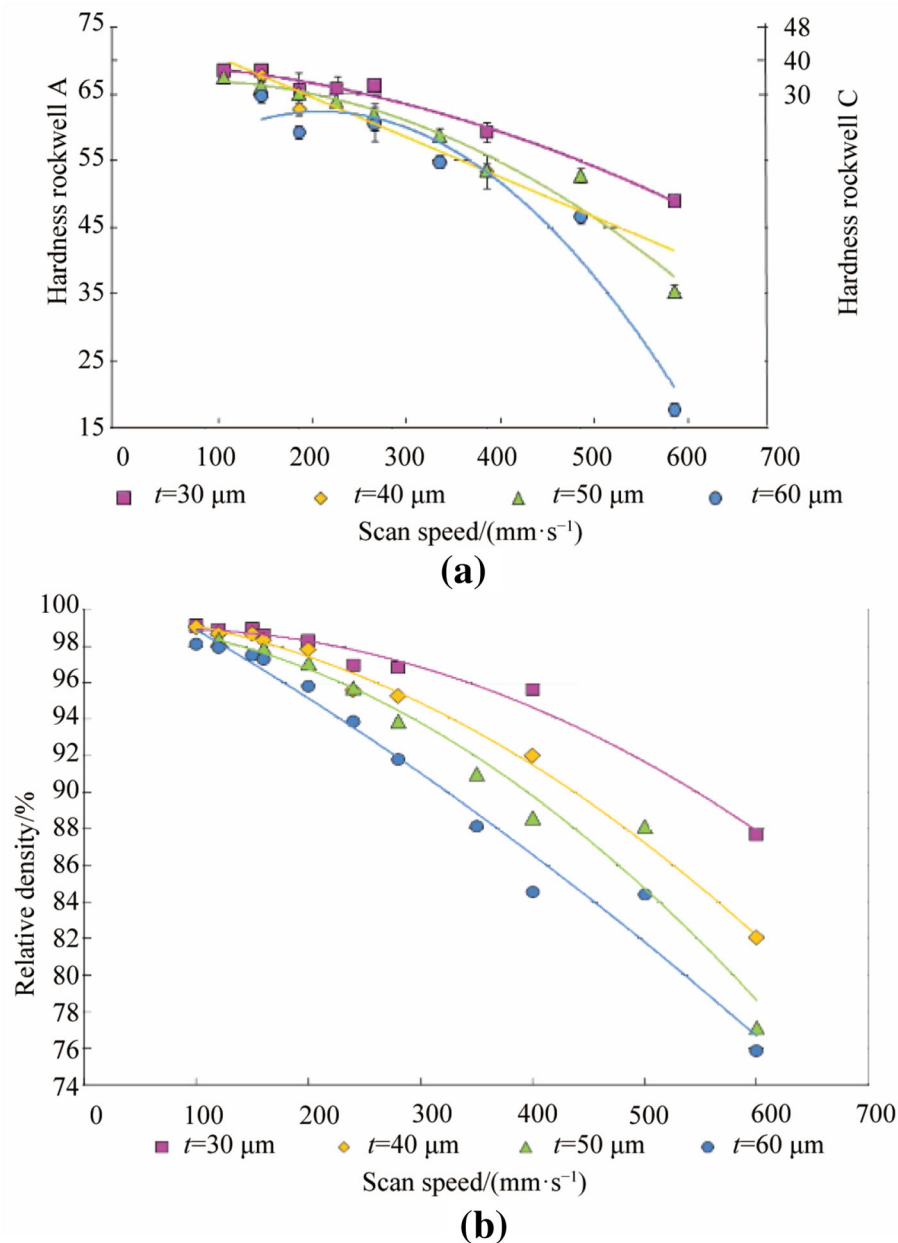


**Fig. 13** **a** Macro-hardness for samples with different scan speeds and layer thicknesses, within a confidence level of 95% for 8 measurements and **b** relative density for samples with different scan speeds and layer thicknesses [116]

high residual stresses were generated compared with the yield strengths of the samples. In addition, they observed that these residual stresses existed from just two additive layers above the substrate and concluded that they might be mainly due to the martensitic transformation that occurred during L-PBF. Ackermann et al. [123] conducted an experimental investigation of the toughness, hardness, and impact properties of H13 manufactured by L-PBF. Samples were analyzed under as-built and heat-treated conditions, and the tensile, hardness, and Charpy test results were compared with the corresponding values for conventionally

generated hot-rolled samples. The authors observed that samples manufactured through L-PBF were more brittle than conventionally created samples even after heat treatment was applied. This is intensified during the AM process owing to the thermal properties of the material.

The influence of AM process parameters on the microstructure and properties of H13 samples has been widely studied. Mazur et al. [9] conducted experimental and numerical studies to quantify the properties, manufacturability, and part characteristics of L-PBF-manufactured H13. Among other findings, the authors concluded

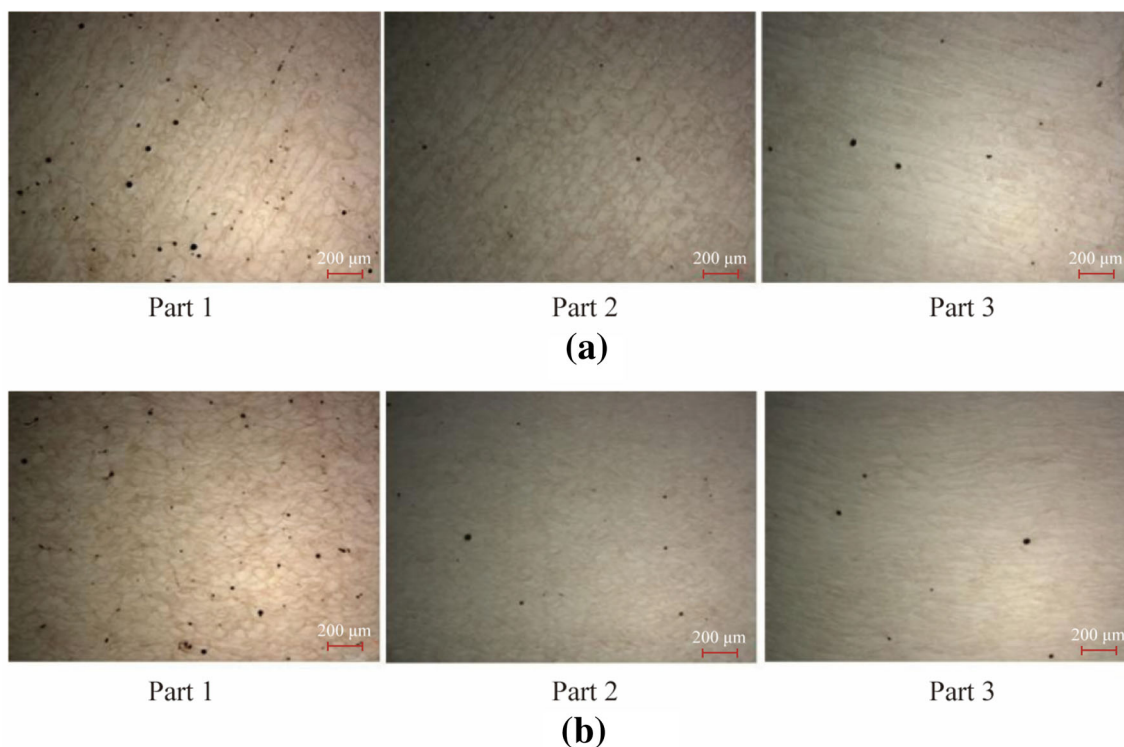


**Fig. 14** Micrographs of **a** top cross-section (cs2) and **b** side cross-section (cs1) [117]

that in L-PBF of H13, a suitable compromise between part porosity and dimensional accuracy could be achieved when the energy density and laser power were set to  $80 \text{ J/mm}^3$  and  $175 \text{ W}$ , respectively. Regarding the energy density, Narvan et al. [124] found that the relative density of parts manufactured through L-PBF increased with increasing energy density up to  $60 \text{ J/mm}^3$ . From this value on, no significant change was observed in the microstructure. In their experiments, samples with a maximum density of 99.7% were obtained. In addition, the authors noted that substrate preheating helped to avoid thermally induced cracks. In 2016, Mertens et al. [126] analyzed the effect of powder preheating on the microstructure, mechanical properties, and residual stresses of H13 samples. During the L-PBF process, they employed a  $170 \text{ W}$  laser power with a beam diameter of  $50 \text{ }\mu\text{m}$ , layer thickness of  $30 \text{ }\mu\text{m}$ , scanning spacing of  $105 \text{ }\mu\text{m}$ , and two scanning speeds of  $400$  and  $800 \text{ mm/s}$ . They compared samples created with no preheating and samples with  $100$ ,  $200$ ,  $300$  and  $400 \text{ }^\circ\text{C}$  pre-heating, and observed that internal stresses on the top surface of samples evolved from compressive without preheating to tensile with preheating at  $400 \text{ }^\circ\text{C}$ . However, they noted that pre-heating at  $400 \text{ }^\circ\text{C}$  led to a uniform bainitic structure that resulted in better mechanical properties.

In addition, the influence of different post-treatments applied to additively manufactured H13 components has

also been studied. Åsberg et al. [127] investigated the effect of stress relief, standard hardening and tempering, and hot isostatic pressing (HIP) on the microstructure, tensile properties, hardness, and porosity of H13 parts generated through an L-PBF technology. During the experiments, a H13 powder particle size within the range of  $15\text{--}45 \text{ }\mu\text{m}$  was employed, and the layer thickness was set to  $30 \text{ }\mu\text{m}$ .  $150 \text{ W}$  laser power and a  $450 \text{ mm/s}$  scanning speed were selected for the contour zone, whereas the laser power and scanning speed were set to  $175 \text{ W}$  and  $720 \text{ mm/s}$ , respectively, for the core of each layer. They observed that the AM H13 material consisted of carbides and ferrite after hardening heat treatment along with colonies of prior austenite. At this stage, the material shows low strength and hardness and a variable elongation to fracture, mainly owing to the porosity. After hardening and tempering, an increase in hardness and strength was noted, and the resulting microstructure was similar to a conventional microstructure, with a martensite structure and carbides. Finally, with the addition of HIP treatment, the highest hardness and ductility values were obtained with a microstructure similar to that conventionally obtained, consisting of tempered martensite and carbides. In addition to maraging steel and H13 alloys, other ferrous alloys such as H11 or H12 have also been used for AM applications. However, as maraging and H13 alloys are the most employed, information about these two materials has been

included in this review. Their behavior is assumed to be representative of the general behavior of other ferrous alloys.

Studies on the evolution of microstructure and mechanical properties of DLD-ed H13 can also be found. In 1997, Mazumder et al. [128] studied the microstructural characteristics and mechanical properties of laser cladding H13. In their experiments, two different deposition modes were employed (fine and coarse) for the deposition of H13 onto an H13 substrate. For the fine mode, a laser spot of 1.1 mm and 4 500 W power was employed, and the powder was fed at 16 g/min. In the case of the coarse deposition mode, the process parameters were set to a laser spot diameter of 0.6 mm, a laser power of 1 000 W, and a powder feed rate of 5 g/min. In both cases, the scanning speed was 750 mm/min. With regard to the microstructure of the generated samples, the authors distinguished four sections: (i) a first section of fully annealed H13 corresponding to the substrate, (ii) a heat-affected zone of the substrate, consisting of tempered martensite, just below the clad layers, (iii) a section of untampered martensite corresponding to the first layer, and (iv) the last section of untampered H13 corresponding to the outermost layers. It is worth noting that as the layers are deposited, heat passes through the layers into the substrate, and section (iii) becomes tempered. The mechanical properties of the generated samples were also analyzed in this work, and it was observed that the average hardness was 690 Knoop and 675 Knoop for the fine and coarse modes, respectively. In addition, the yield strength of the samples was 1 505 MPa, and the ultimate strength was 1 820 MPa. Similar results were obtained by other authors [125, 129, 130] with regard to the resulting microstructure. Pinkerton and Li [129] analyzed the feasibility of using water-atomized powder particles as an alternative to gas-atomized powder. They observed that in both cases, the wall samples created had a martensitic structure with a small amount of austenite in the upper layers. Moving down the wall, untampered, transition, and tempered regions were observed. In addition, they found that samples created by gas-atomized powder were harder than those created by water-atomized powder. Xue et al. [130] also deposited H13 powder using a 1 kW laser power. In addition to the dominant martensitic microstructure with some amount of austenitic phase, the authors observed that the samples created were crack-free and had a fine microstructure, possibly due to the process-induced rapid solidification. They also observed that the mechanical properties (tensile strength, strain, and sliding wear resistance) measured in the samples were comparable to those of wrought H13. Moreover, Cottam et al. [122] analyzed the microstructure and residual stresses generated on a wedge-shaped H13 sample manufactured by DLD. They employed a 2 500 W laser power, 300 mm/min

traversing speed, and powder fed at 4.5 g/min. As previously reported, they observed that the phase transformation occurring during the deposition processes greatly affected the final microstructure of the sample and in turn the residual stress distribution. The wedge-shaped sample showed a martensitic microstructure and a tempering evolution from the outer surface to the interior. In addition, the authors observed that a high hardness and compressive stresses were generated on the top 4 mm of the wedge, which were suitable for die casting and forging dies. The samples also showed good resistance to thermal fatigue. Park et al. [131] analyzed the influence of energy input on the microstructure, hardness, and chemical composition of H13 samples. In their experiments, samples were created by DLD technology with 2 kW laser power, 0.56 mm beam, and powder feed rate of 0.057 g/s. The energy input was varied within the range of 37.81–88.21 J/mm<sup>2</sup>. The resulting microstructure was a mixed cell type and a dendritic structure. The authors also observed that large-sized grains were generated as a consequence of the low cooling rate caused by the high energy input. It was observed that the hardness decreased with the increased energy input, which could be due to microstructure coarsening and the decrease in carbon content. Finally, the authors noted that energy input had no significant effect on the chemical composition.

The results obtained through the AM of H13 by WAAM technology were also analyzed. Wang et al. [132] employed additive WAAM technology, specifically MIG, to generate thin-walled samples and observed that different thermal histories resulted in different microstructures. However, they noted that the hardness of the generated samples was uniform from the top to the bottom of the walls. The authors observed anisotropy in the mechanical properties of the as-welded samples. However, these properties became isotropic after heat treatment by annealing at 830 °C for 4 h. Recently, Ge et al. [133] investigated the characteristics of H13 samples generated by the so-called cold metal transfer, which was a novel WAAM technology. Optimal process parameters were selected from preliminary tests: a 0.15 m/min deposition speed, 12.7 V and 118 A deposition voltage and current, a wire feed speed of 8 m/min, a 90° wire feed angle, and a 5.5 mm distance between successive deposition tracks. They observed that a negligible porosity was generated at below 0.001%, which ensured a sound metallurgical bonding in the as-deposited part. In addition, good microhardness values were measured in the body zone. An enhanced ultimate tensile strength was obtained regarding the mechanical properties owing to the generation of a hard martensite structure.

## 4.2 Non-ferrous alloys

### 4.2.1 Properties of AM Co-Cr-W alloys

Co-Cr-W alloys are particularly suitable for tooling applications requiring high wear resistance, toughness, and high-temperature hardness that other tooling materials, such as conventional carbides or high-speed steels, do not provide. Because this work focuses on additively manufactured tool materials, in this section, among other Co-based alloys, the properties of additively manufactured Stellite™ alloys are reviewed owing to their common use in AM processes. Stellite™ alloys are primarily used in DLD processes for the remanufacturing of industrial components (crankshafts, shafts, and turbine blades) [48, 134–138]. Stellite™ alloys are among the so-called superalloys. As mentioned, they are Co-based alloys that contain a high amount of chromium (20%–30% (mass fraction)), Tungsten (4%–18% (mass fraction)), Molybdenum and carbon (0.25%–3% (mass fraction)) [139]. Stellite™ alloys have also been chosen as tool materials for machining stainless steel owing to their weldability, properties, and powder availability. These alloys provide excellent mechanical wear resistance at high temperatures (up to 500 °C) and exhibit outstanding corrosion, erosion, abrasion, and galling resistance [140, 141]. In addition, Stellite™ shows good resistance to sliding wear when employed in forging and forming applications [142, 143]. They represent a good alternative to H13 steel, which is traditionally employed to manufacture dies [144]. Owing to their excellent formability, weldability, and combination of good wear resistance and high-temperature strength, Stellite™ alloys are also used as coatings for bearings, pump seals, knives, and valve seats [145, 146].

In the following section, a review of the most relevant studies concerning the microstructural and mechanical properties of additively manufactured Stellite™ are presented.

Many research studies concerning the AM of Stellite alloys through laser cladding have been recently reported [147–150]. Sun et al. [151] deposited Stellite 6 on a stainless-steel substrate through laser cladding by using a pulsed laser with frequencies within the range of 40–60 Hz and a fixed pulse length of 8 ms. Different hardness values were measured in samples that depend on the process conditions. They observed that crack formation could be avoided by employing multi-track cladding owing to the remelting of cracks in the subsequent tracks. The same process was tested by Singh et al. [152], who conducted laser cladding experiments of Stellite 6 on stainless steel substrates using different energy density values (within the range of 32–52 J/mm<sup>2</sup>). The authors employed a laser spot

of 4 mm, a scanning rate of 10 mm/s, and a 30% overlap between successive scanning tracks and observed that the lowest energy density tested, that is, 32 J/mm<sup>2</sup>, led to a higher hardness of the samples, which decreased with an increase in the energy density. Yao et al. [139] compared the performance of Stellite 21 alloy with Stellite 22 and Stellite 728 through the deposition of materials on a 316 stainless steel substrate using laser cladding. Stellite 22 and Stellite 21 powders had similar compositions. Stellite 728 powder has a slightly higher carbon content than Stellite 21 powder, as well as Nb. During these tests, the laser power was set to 1 800 W with a spot size of 4 mm, an energy density of 75 J/mm<sup>2</sup>, a laser scanning rate of 6 mm/s, and a powder feeding rate of 13 g/min. As a result of their experiments, Yao et al. [139] observed that Stellite 728 exhibited the highest hardness. According to the wear resistance, Stellite 22 and Stellite 728 exhibit approximately 2- and 3-times higher wear resistance, respectively, than Stellite 21. Diaz et al. [153] employed Stellite alloys (concretely, 6, 12 and 21 alloys) and Triballoys® to repair Cr-Mo steel components by laser cladding with a maximum laser power of 2 200 W during their experiments. N<sub>2</sub> inert gas was also employed as the shielding and powder carrier gas. When using Stellite alloys, they noted that dendritic microstructures were generated, and coating with neither cracks nor porosity could be deposited. In addition, they remarked that crack-free deposition can be enhanced by preheating the substrate material. AM of Stellite alloys has also been applied to the generation of functionally graded materials (FGMs) through the combination of different metallic substances. Ding et al. [146] also conducted experimental research with the aim of improving the characteristics and properties of Stellite 3 and Stellite 6 laser cladding samples by mixing Stellite 3 (70%) and Stellite 21 (30%). They compared the results to Stellite 3 and Stellite 6 samples, and observed that, given the optimal process parameters, mixed material samples showed better microstructural characteristics and no cracking. Therefore, they concluded that this mixture of materials could be employed for property enhancement in terms of hardness, wear resistance, and laser processing.

Direct laser deposition technology has also been employed for the manufacturing of Co-Cr-W alloys. Traxel and Bandyopadhyay [154] compared the performance of the Stellite 6 machining tool produced by the LENS AM technology with a commercially available tool. They observed that the capability of the AM Stellite tool was comparable to that of a commercially available tool. They also found that laser re-melting of the Stellite enabled a slight increase in the surface hardness. The same Stellite alloy was the object of research conducted by Moradi et al. [143]. In their work, the authors investigated the influence

of the laser's focal position and its power on the geometrical dimensions, microhardness profile, grain size, and microstructure of additively manufactured Stellite 6 alloys. The powder particle size employed was 10–36  $\mu\text{m}$ , and the DLD parameters were set as follows: 1 kW laser power with a minimum spot size of 0.2 mm, a focal length of 200 mm, and a Rayleigh length of 2 mm operated in a continuous wave. During these tests, the cobalt-based Stellite alloy was deposited on a DIN1.2714 hot work tool steel substrate. The authors observed that grain size increases with an increase in the laser power, leading to grain sizes of 3.13 and 2.11  $\mu\text{m}$  when using the highest and lowest laser power values, respectively. An inverse trend was observed for the microhardness of the generated samples. For laser power that leads to the smallest grain size, the highest microhardness values were reported. It is worth noting that the microhardness of the samples was higher at the center of the samples than at the beginning and end of the deposited walls. Ren et al. [155] analyzed the influence of heat treatment on the microstructure of additively manufactured Stellite 12 samples by comparing the hardness and wear resistance at high temperatures of untreated and heat-treated samples. Three different treatment processes were analyzed: solution heat treatment, aging, and the combination of both. Table 2 summarizes the process parameters employed during the tests.

The authors observed that the highest hardness corresponded to the samples after aging. However, such samples also exhibited the worst wear resistance. They noted that wear resistance could be improved by applying heat treatment, and samples subjected to the combination of solution heat treatment and ageing exhibited the best performance against wear resistance.

As mentioned above, one of the applications of Stellite alloys is the repair and remanufacturing of forging dies. Foster et al. [144] employed DLD to repair H13 dies with Stellite 21 alloy with a 500 W laser power, scanning speed of 12 mm/s, and argon as a carrier and shielding gas. Among the Stellite alloys, Stellite 21 contains the lowest

carbon content. It provides a high mechanical strength at high temperatures and good corrosion resistance, making it suitable for applications such as forging or hot stamping dies and valve trims for high-pressure steam, oil, and petrochemical processes [139]. The authors observed that the additively manufactured Stellite 21 shows a better performance in terms of wear resistance. In addition, it provides a good toughness, machinability, and forge-ability for the application considered in this study. The feasibility of FGM using DLD technology was also tested. Muller et al. [156] analyzed the capability of DLD technology for the generation of FGM samples by combining 316 L stainless steel and Stellite 6. The material gradient was established in the direction perpendicular to the substrate, and a scanning speed of 900 mm/min and a laser power of 256 W were employed. Pore-free and crack-free FGM samples can be generated using this combination of materials and the aforementioned process.

#### 4.2.2 Properties of AM W-C alloys

Among the W-C alloys, tungsten carbide-cobalt (WC-Co) is one of the most widely used materials for wear-resistant parts, cutting tools, and molds. WC-Co cermet with a Co content of 5%–25% (mass fraction) possesses superior hardness, compressive strength, fracture toughness, and transverse rupture strength. In addition, WC-Co exhibits high wear properties and good corrosion resistance. WC-Co has been traditionally produced by injection molding, extrusion molding, and powder metallurgy. However, these processes are inefficient and expensive. In this context, AM technologies are an excellent alternative to traditional processes in terms of productivity and enable the generation of complex geometries and internal cooling channels [157]. However, AM of WC-Co alloys is extremely complicated, mainly because of the different melting temperatures and optical absorptance of the laser beam wavelength of WC and Co and the fragility of WC, which when considering the thermal cycles in the AM processes, is an important issue [158]. A summary of the relevant literature regarding the AM of WC-Co alloys is presented in the following section.

Most studies analyzing the characteristics of additively manufactured W-C alloys have employed L-PBF technology. Chen et al. [159] employed L-PBF AM technology to generate bulk cemented carbide, and they observed that relatively high-density samples can be obtained (at more than 96%). They analyzed in detail the influence of grain morphology on the microstructure generated. During their experiments, the authors employed a laser power within the range of 380–400 W, with a spot size of 80  $\mu\text{m}$ . A scanning speed of 470–500 mm/s was also selected, and the hatching space and powder layer thickness were set to

**Table 2** Process parameters [155]

Parameter	Value
Laser power/W	3 000
Powder size/ $\mu\text{m}$	25–86
Travel speed/(mm·s <sup>-1</sup> )	8
Powder flow rate/(g·min <sup>-1</sup> )	18
Carrier gas flow rate/(L·min <sup>-1</sup> )	5
Protective gas flow rate/(L·min <sup>-1</sup> )	15
Overlapping rate/%	45
Z step/mm	0.9

60–75  $\mu\text{m}$ . The authors observed that spherical granules lead to higher densities owing to their higher apparent density. In the cross-section parallel to the laser beam, the lamellar microstructure was prominent with both coarse and fine WC grains, whereas in the horizontal cross-section, no lamellar structure was observed. Regardless of the anisotropic microstructure, the hardness obtained was similar in both the vertical and horizontal directions. Domashenkov et al. [160] compared the microstructure and mechanical properties of WC/Co12 samples generated by L-PBF using conventional and nanocomposite powders. The aim of their study was to analyze the effect of the initial crystallite size on the microstructure and mechanical properties. The authors observed that both coarse and fine carbide samples were segregated in the molten pool. The sample made from the nano-phased powder showed higher homogeneity in terms of the microhardness. Uhlmann et al. [161] also compared the results obtained in the L-PBF of WC-Co when using two different powders. In this study, agglomerated and pre-sintered powders were employed to analyze the evaporation effect during the L-PBF process. The authors noted that a high energy density results in a coherent and closed molten pool and leads to a high density. However, it also generates the embrittlement of tungsten carbide, which in turn enables the thermally induced cracks to spread. By contrast, a low energy density leads to a higher porosity. Fortunato et al. [158] generated WC-Co samples by L-PBF using 80 W laser power, a spot diameter of 50  $\mu\text{m}$ , and a scanning speed of 400 mm/s. After the AM process, the samples were subjected to the

HIP treatment. They showed that the density of the samples increased with increasing energy density until a certain energy density (375  $\text{J}/\text{mm}^3$  in these experiments) was reached. Similar results were obtained by Ku et al. [162] for L-PBF samples generated with varying processing parameters. In their experiments, the authors varied the laser power from 40 to 75 W and employed two different scanning speeds (75 and 150 m/s) and hatching spaces (50 and 75  $\mu\text{m}$ ), and the layer thickness was set to 30  $\mu\text{m}$  in all tests. In Fig. 15, as extracted from this study, it can be observed that a decrease in energy density yields a decrease in the generated sample density.

Regarding the chemical composition, the importance of Co as a binder was confirmed in this study. The greater the quantity of Co that is applied, the lower the brittleness of the components. Additionally, a low Co content leads to the generation of porous samples. Regarding the influence of Co content on the achieved results, Khmyrov et al. [163] studied the range of the WC/Co ratio needed to ensure that cracks are avoided. In their experiments, laser power from 50 W to 100 W was employed with a spot diameter of 100  $\mu\text{m}$ , and the scanning speed was varied from 10 to 100 mm/s. The authors concluded that by using a powder mixture with 25% (mass fraction) WC during L-PBF process, samples without cracks could be generated. The same AM technology was employed by Li et al. [164] to create cemented carbide alloy samples composed of an 80% (mass fraction) spherical tungsten carbide powder mixed with 20% (mass fraction) gas-atomized NiAlCoCrCuFe high-entropy alloy powder. Optimized process parameters

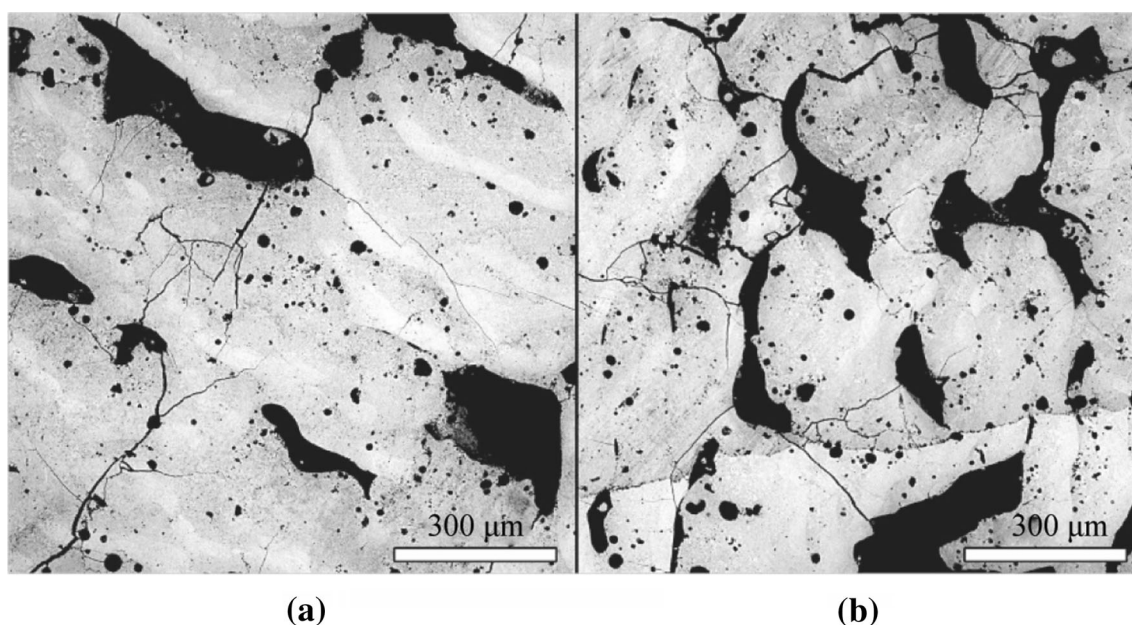


**Fig. 15** Density of L-PBF samples for different energy densities **a** energy density 16  $\text{J}/\text{mm}^2$  and density 95% and **b** energy density 13.33  $\text{J}/\text{mm}^2$  and density 91.8% [162] (The figures are reused under the Creative Commons Attribution License.)

were obtained for the manufacturing, that is, a 140-W laser power, 90-mm/s scan speed, 115- $\mu\text{m}$  hatch distance, and 40- $\mu\text{m}$  layer thickness. The hardness and toughness of the generated samples varied because of the microstructural heterogeneity of the cemented carbide. In addition, a variety of chemical compositions and microstructures of the samples were observed along the building direction owing to the diffusion from the baseplate materials and element evaporation caused by the high laser power employed. Both the hardness values and fracture toughness of the samples increased along the building direction. Gu [165] employed L-PBF to generate W-Ni-graphite samples with two different laser types: a CO<sub>2</sub> laser and a fiber laser. They obtained high-density parts (up to 96.3%) and observed that by increasing the laser power or decreasing the scanning speed, a coarsening of WC crystals in both the length side and thickness of the samples occurred.

Few studies have been published on the mechanical properties of additively manufactured non-ferrous alloys. Concerning the AM of these alloys through L-PBF, Yang et al. [157] conducted a review of AM of WC-Co hard metals, where they summarized the main conclusions extracted from the literature with regard to the AM of such non-ferrous alloys. Among other characteristics, they analyzed the hardness and fracture toughness. Concerning the hardness of additively manufactured non-ferrous alloys, Yang et al. [157] mentioned that the resultant hardness was uneven when using L-PBF, and thus so was the structure of the sample. The addition of Cr to WC-Co enhances the hardness, limiting the growth of WC grains. According to their review, an efficient process for improving the characteristics of WC-Co samples is to minimize the WC grain size. It has been shown that small grain sizes can produce high hardness and resistance to wear. However, it also decreases the toughness. In their study, it was concluded that L-PBF samples have a higher hardness but lower toughness than samples generated through other technologies such as BJ or fused filament fabrication. This is due to the uneven distribution of heat in the L-PBF process, leading to Co evaporation and a ternary phase transformation. This can make the sample tougher and brittle at the same time.

As for DLD-ed W-C alloy, Hutasoit et al. [142] analyzed the microstructure and mechanical properties on the interface between an AISI 4130 steel substrate and laser clad Stellite 6. Stellite grain size was within the range of 45–150  $\mu\text{m}$ , and during the deposition, a 550-W laser power was employed with a spot diameter of 3 mm. The scanning speed was set to 500 mm/min, the powder feed was 4 g/min, and the nozzle was inclined at 60°. Argon was employed as the shielding gas. The authors defined two distinctive zones: the dilution, where the substrate melts with the coating and has a similar microstructure, and the

heat-affected zone, which is in the substrate but has a different microstructure. They observed that the heat-affected zone has a lower elastic modulus than the dilution section.

Table 3 presents a summary of the main conclusions presented in the previous sections regarding the microstructural and mechanical properties of AM tooling alloys [108, 111–117, 122–125, 127–133, 139, 143, 144, 151–155, 158–161, 164–166].

## 5 Conclusions

In this study, a review and analysis of the relevant literature regarding AM technologies of tooling alloys was presented. The properties and characteristics of tooling alloys were first reviewed, considering the demands of the industry. Powder bed fusion, directed energy deposition, BJ, and material extrusion, which are the most employed methods in the tooling industry, were also presented. Next, the microstructural and mechanical properties of tooling alloys that can be achieved through AM processes were analyzed. Special emphasis has been placed on materials that are usually employed in the tooling industry when considering ferrous (maraging steel and H13 steel alloy) and non-ferrous (Stellite and WC-Co) alloys. Finally, the influence of the AM parameters on the density, microstructure, and mechanical properties of the resulting samples was analyzed.

The review shows that steel-based tooling alloys can be processed well using AM, and some steels show better properties than conventionally produced steels such as maraging steels. However, in some cases, such as high-carbon steel grades possess micro-cracks and porosity. As shown in the literature, the microstructure of AM-produced steel tooling alloys is dominated by solidification and a solid-state phase transformation.

AM technologies offer attractive advantages for producing tooling alloys with complex geometries. These complex shapes with internal cooling channels allow higher manufacturing speeds and, as a result, a remarkable increase in process productivity. However, manufacturing fully dense high integrity tools using AM is still a challenging and iterative process.

It has been shown that additive process parameters have a significant influence on the microstructure of generated parts, as phase transformations might be induced during manufacturing owing to the large amount of heat generated. According to the energy density, a balance must be found to obtain the best results in terms of the density and hardness of the parts. As previously shown, the density and hardness of AM parts increase with an increase in energy density up to a point. Excessive energy density input may

**Table 3** Summary of most relevant remarks regarding the microstructure and mechanical properties of additively manufactured tooling materials

Type	Material	Alloy	AM technology	Microstructural properties	Mechanical properties	Ref.		
Ferrous	Maraging steels	18Ni-300/1.2709	L-PBF and DLD	DLD samples show the highest hardness due to intrinsic heat-treatment	Properties comparable to those of conventionally manufactured maraging steels. In fact, L-PBF technology have shown higher yield and ultimate tensile strength in the non-treated form	[112]		
			L-PBF	As laser energy increases, porosity decreases up to a certain point and then increases		[113, 114]		
				High energy density values lead to higher porosity				
				Scanning strategy has a considerable effect on porosity. Double exposure scanning strategy enables the generation of parts with higher density			[115]	
				Part density decreases with increasing layer thickness and so does the macro-hardness			[116]	
				Laser re-melting enables the generation of parts with lower porosity			[117]	
						Part orientation and heat-treatment have an influence on the mechanical properties. #Untreated samples suffered significant plastic deformation before breakage. #Annealed samples showed lower yield strength and higher ductility	[111]	
H13	—		Laser cladding	Four sections can be distinguished:		[128]		
			DLD	Fully annealed		[108]		
			DLD	Heat affected, tempered martensite		[130]		
			L-PBF	Un-tempered martensite. Un-tempered H13 (outermost layers)		[125]		
			DLD	Final microstructure highly affected by the phase transformation that occurs during deposition		[122]		
				Martensitic microstructure along with tempering evolution is observed				
			DLD	Mixed cell-type and dendritic microstructure with large-sized grains due to low cooling rate (high energy density)			[131]	
				Hardness decreases with the increase in energy density, which might be due to microstructural coarsening and decrease in carbon content				
			L-PBF	L-PBF samples more brittle than conventional		[123]		
			WAAM (MIG)	Different thermal history leads to different microstructure. However, hardness is uniform		[132]		
L-PBF	Relative density increases with increasing energy density up to a point. Substrate pre-heating helps in avoiding thermally induced cracks		[124]					
WAAM (cold metal transfer)	Negligible porosity and good microhardness values are generated	Enhanced UTS due to the generation of hard martensite microstructure	[133]					
L-PBF	After hardening treatment (HT), H13 consists of carbides, ferrites and prior austenite and shows low strength and hardness		[127]					
	After HT + Tempering strength and hardness increase							
	After HT + Tempering + HIP: samples consist of tempered martensite and highest ductility and hardness values are obtained							

**Table 3** continued

Type	Material	Alloy	AM technology	Microstructural properties	Mechanical properties	Ref.	
Non-ferrous	Co-Cr-W	Stellite 6	LENS	Laser re-melting enables slight increase on surface hardness		[154]	
			DLD	Grain size increases with an increase in laser power. The trend inverse for hardness		[143]	
			Laser cladding	Crack formation can be avoided by multi-track scanning because it induces re-melting of cracks		[151]	
				Laser cladding	Increase in energy density leads to decrease in hardness		[152]
			Stellite 12	DLD	Among different post-treatments, aging leads to highest hardness values. Solution heat-treatment + aging leads to highest wear resistance		[155]
			Stellite 21	DLD	Shows better wear resistance		[144]
			Stellite 21, 22 and 728	DLD	Stellite 728 shows highest hardness Stellite 22 and 728 show higher wear resistance		[139]
			Stellite 6, 12 and 21	Laser cladding	Dendritic microstructures are generated free of cracks and without porosity. This can be enhanced by pre-heating the substrate		[153]
			WC	WC-Co	L-PBF	Grains with spherical shape lead to higher density samples Lamellar microstructure in the vertical direction (parallel to the laser beam) and no lamellar microstructure in the horizontal cross-section	Despite of the anisotropic microstructure, similar hardness was obtained in both horizontal and vertical directions
	L-PBF	Both samples coarse and fine carbides segregate in the molten pool			Samples created from the nanocomposite powder show higher microhardness homogeneity	[160]	
		WC-Co agglomerated and pre-sintered powder		L-PBF	High energy density may lead to embrittlement and, in turn, to the propagation of cracks. However, low energy density leads to porosity Density of samples increases with increasing energy density, before reaching a horizontal asymptote for a certain energy density. The importance of Co is highlighted. The greater the quantity of Co, the lower the brittleness of components. Additionally, low Co content leads to the generation of porous samples		[161] [158]
		WC-Co-Cr		L-PBF	Small cracks and high-density samples	Hardness values show high deviation due to the variability of WC grain sizes employed in the experiments	[166]
		WC-NiAlCoCrCuFe	L-PBF	Variation of chemical composition and microstructure of samples was observed along the building direction due to the diffusion from baseplate materials and element evaporation	Hardness and fracture toughness increased in the building direction	[164]	
	W-Ni-graphite	L-PBF	Grain coarsening occurs when increasing laser power or decreasing scanning speed		[165]		

lead to low density and decreased hardness. In addition, the layer thickness has a similar influence on the part density because this property decreases with the increase in the layer thickness employed. It is worth noting that various authors have observed that preheating of the substrate and powder material has a beneficial effect on the properties of the manufactured parts.

As a result of the literature analysis conducted in this review paper, it was observed that the mechanical

properties of additively manufactured tooling alloys have not yet been deeply analyzed, particularly the additive manufacturing of non-ferrous alloys such as Co-Cr-W and W-C. Considering the applications of such alloys in the tooling industry, it is clear that such an analysis must be addressed in the near future to better apply AM in the tooling industry. It was shown that exposure of WC-Co to high-energy laser/electron beams might result in a decarburization of WC, carbide formation such as  $W_2C$ , and

possible evaporation of Co, which might have detrimental effects on the properties of the final parts. Therefore, further efforts are required to eliminate this phenomenon.

Although it is a promising alternative to conventional manufacturing processes, the AM of tooling alloys still presents some challenges that must be addressed. Some of the issues, such as the surface quality and porosity of the parts, are common to the additive manufacturing of any material. This, in turn, may affect the microstructure and mechanical properties of the components. Therefore, the process parameters must be optimized for each material and additive technology employed to ensure the best results. In particular, in the additive manufacturing of tooling alloys, it has been observed that phase transformations that occur during the process owing to the large amount of heat generated is a major concern, affecting the mechanical behavior of the generated components.

The review and analysis presented in this paper demonstrate that the AM of tooling alloys needs further investigation to completely integrate such technologies in the tooling industry and production plants. With this aim, the impact behavior, fatigue life, and failure of tooling components generated or repaired through AM must be investigated. In addition, to improve the confidence of the industry in applying AM to their production lines, it is necessary to develop numerical models that help in understanding the physics of the processes and to optimize the parameters and obtain the required qualities in the built components. Considering the benefits that additive manufacturing can provide to this industry, the authors encourage the research community to continue their investigations into these matters.

**Open Access** This article is licensed under a Creative Commons Attribution 4.0 International License, which permits use, sharing, adaptation, distribution and reproduction in any medium or format, as long as you give appropriate credit to the original author(s) and the source, provide a link to the Creative Commons licence, and indicate if changes were made. The images or other third party material in this article are included in the article's Creative Commons licence, unless indicated otherwise in a credit line to the material. If material is not included in the article's Creative Commons licence and your intended use is not permitted by statutory regulation or exceeds the permitted use, you will need to obtain permission directly from the copyright holder. To view a copy of this licence, visit <http://creativecommons.org/licenses/by/4.0/>.

## References

- Merklein M, Junker D, Schaub A et al (2016) Hybrid additive manufacturing technologies: an analysis regarding potentials and applications. *Phys Procedia* 83:549–559
- Essa K, Hassanin H, Attallah MM et al (2017) Development and testing of an additively manufactured monolithic catalyst bed for HTP thruster applications. *Appl Catal A Gen* 542:125–135
- Sabouri HBA, Yetisen AK, Sadigzade R et al (2017) Three-dimensional microstructured lattices for oil sensing. *Energy Fuels* 31:2524–2529
- Li S, Hassanin H, Attallah MM et al (2016) The development of TiNi-based negative Poisson's ratio structure using selective laser melting. *Acta Mater* 105:75–83
- Hassanin H, Alkendi Y, Elsayed M et al (2020) Controlling the properties of additively manufactured cellular structures using machine learning approaches. *Adv Eng Mater* 22:1–9
- Hassanin H, Finet L, Cox SC et al (2018) Tailoring selective laser melting process for titanium drug-delivering implants with releasing micro-channels. *Addit Manuf* 20:144–155
- Yasa E, Poyraz O, Cizioglu N et al (2015) Repair and manufacturing of high performance tools by additive manufacturing. In: The 8th international conference and exhibition on design and production of machines and dies/molds, Kuşadası, Aydın, Turkey
- Bajaj P, Hariharan A, Kini A et al (2019) Steels in additive manufacturing: a review of their microstructure and properties. *Mater Sci Eng A* 772:138633. <https://doi.org/10.1016/j.msea.2019.138633>
- Mazur M, Leary M, McMillan M et al (2016) SLM additive manufacture of H13 tool steel with conformal cooling and structural lattices. *Rapid Prototyp J* 22(3):504–518
- Nee AYC (2015) Handbook of manufacturing engineering and technology. Springer, London
- Shah M, Unanue L, Bidare P et al (2010) Tool control monitoring applied to drilling. In: Proc. 6th MUGV conference, Cluny, 13–15 Oct
- Kruth JP, Froyen L, Van Vaerenbergh J et al (2004) Selective laser melting of iron-based powder. *J Mater Process Technol* 149(1/3):616–622
- Frazier WE (2014) Metal additive manufacturing: a review. *J Mater Eng Perform* 23(6):1917–1928
- Selcuk C (2011) Laser metal deposition for powder metallurgy parts. *Powder Metall* 54(2):94–99
- 3D hubs. Producing metal parts: CNC vs. additive manufacturing. HUBS company, Amsterdam
- Manogharan G, Wysk R, Harrysson O et al (2015) AIMS-a metal additive-hybrid manufacturing system: system architecture and attributes. *Procedia Manuf* 1:273–286
- Tofail SAM, Koumoulos EP, Bandyopadhyay A et al (2018) Additive manufacturing: scientific and technological challenges, market uptake and opportunities. *Mater Today* 21(1):22–37
- Additive Manufacturing Research Group (2020) About additive manufacturing: directed energy deposition. <https://www.lboro.ac.uk/research/amrg/about/the7categoriesofadditivemanufacturing/directedenergydeposition>
- King WE, Anderson AT, Ferencz RM et al (2015) Laser powder bed fusion additive manufacturing of metals; physics, computational, and materials challenges. *Appl Phys Rev* 2(4):41304. <https://doi.org/10.1063/1.4937809>
- Das S (2003) Physical aspects of process control in selective laser sintering of metals. *Adv Eng Mater* 5(10):701–711
- Mohammed MT (2018) Mechanical properties of SLM-titanium materials for biomedical applications: a review. *Mater Today Proc* 5(9):17906–17913
- Igor S (2019) Aerospace applications of the SLM process of functional and functional graded metal matrix composites based on NiCr superalloys. In: Froes F, Boyer R (eds) Additive manufacturing for the aerospace industry, Elsevier, Amsterdam, pp 265–281
- Jiménez A, Bidare P, Hassanin H et al (2021) Powder-based laser hybrid additive manufacturing of metals: a review. *Int J Adv Manuf Technol* 114:63–96

24. Gu DD, Meiners W, Wissenbach K et al (2012) Laser additive manufacturing of metallic components: materials, processes and mechanisms. *Int Mater Rev* 57(3):133–164
25. Liverani E, Toschi S, Ceschini L et al (2017) Effect of selective laser melting (SLM) process parameters on microstructure and mechanical properties of 316L austenitic stainless steel. *J Mater Process Technol* 249:255–263
26. Read N, Wang W, Essa K et al (2015) Selective laser melting of AlSi10Mg alloy: process optimisation and mechanical properties development. *Mater Des* 65:417–424
27. Bidare P, Maier RRJ, Beck RJ et al (2017) An open-architecture metal powder bed fusion system for in-situ process measurements. *Addit Manuf* 16:177–185
28. Bidare P, Bitharas I, Ward RM et al (2018) Fluid and particle dynamics in laser powder bed fusion. *Acta Mater* 142:107–120
29. Ferrar B, Mullen L, Jones E et al (2012) Gas flow effects on selective laser melting (SLM) manufacturing performance. *J Mater Process Technol* 212(2):355–364
30. Seabra M, Azevedo J, Araújo A et al (2016) Selective laser melting (SLM) and topology optimization for lighter aerospace components. *Procedia Struct Integr* 1:289–296
31. Tang L, Wu C, Zhang Z et al (2016) A lightweight structure redesign method based on selective laser melting. *Metals* 6(11):280. <https://doi.org/10.3390/met6110280>
32. Renishaw PLC (2017) RenAM 500Q multi-laser AM system. <https://resources.renishaw.com/en/details/data-sheet-renam-500q-99032>
33. Qiu C, Adkins NJE, Hassanin H (2015) In-situ shelling via selective laser melting: modelling and microstructural characterization. *Mater Des* 87:845–853
34. Hassanin H, Essa K, Qiu C et al (2017) Net-shape manufacturing using hybrid selective laser melting/hot isostatic pressing. *Rapid Prototyp J* 23(4):720–726
35. Additive Industries (2015) Tailor-made for your operation: the modular and scalable MetalFAB1. <https://www.additiveindustries.com/systems/metalfab1>. Accessed 17 Mar 2020
36. Bidare P, Bitharas I, Ward RM et al (2018) Laser powder bed fusion at sub-atmospheric pressures. *Int J Mach Tools Manuf* 130(131):65–72
37. Bidare P, Bitharas I, Ward RM et al (2018) Laser powder bed fusion in high-pressure atmospheres. *Int J Adv Manuf Technol* 99(1/4):543–555
38. GE Additive (2015) Concept laser. <https://www.ge.com/additive/de/who-we-are/concept-laser>. Accessed 06 Apr 2020
39. EOS (2017) EOSTATE monitoring and quality assurance - real-time monitoring for industrial 3D printing. <https://www.eos.info/software/monitoring-software>. Accessed 06 Apr 2020
40. Graff HKP, Ståhlbom B, Nordenberg E et al (2016) Evaluating measuring techniques for occupational exposure during additive manufacturing of metals: a pilot study. *J Ind Ecol*. <https://doi.org/10.1111/jiec.12498>
41. Yadroitsev I, Bertrand P, Smurov I (2007) Parametric analysis of the selective laser melting process. *Appl Surf Sci* 253(19):8064–8069
42. Mumtaz KA, Erasenthiran P, Hopkinson N (2008) High density selective laser melting of waspaloy. *J Mater Process Technol* 195(1/3):220–232
43. Spierings AB, Herres N, Levy G (2011) Influence of the particle size distribution on surface quality and mechanical properties in AM steel parts. *Rapid Prototyp J* 17(3):195–202
44. Liu B, Wildman R, Tuck C et al (2011) Investigation the effect of particle size distribution on processing parameters optimisation in selective laser melting process. In: The 22nd annual international solid freeform fabrication symposium: an additive manufacturing conference, Austin, pp 227–238
45. Yadroitsev I, Thivillon L, Bertrand P et al (2007) Strategy of manufacturing components with designed internal structure by selective laser melting of metallic powder. *Appl Surf Sci* 254(4):980–983
46. Simonelli M, Tuck C, Aboulkhair NT et al (2015) A study on the laser spatter and the oxidation reactions during selective laser melting of 316L stainless steel, Al-Si10-Mg, and Ti-6Al-4V. *Met Mater Trans A* 46:3842–3851
47. King WE, Anderson AT, Ferencz RM et al (2015) Laser powder bed fusion additive manufacturing of metals; physics, computational, and materials challenges. *Appl Phys Rev* 2(4):41304. <https://doi.org/10.1063/1.4937809>
48. Thompson SM, Bian L, Shamsaei N et al (2015) An overview of direct laser deposition for additive manufacturing; Part I: transport phenomena, modeling and diagnostics. *Addit Manuf* 8:36–62
49. Löffler K (2013) Developments in disk laser welding. In: Katayama S (ed) *Handbook of laser welding technologies*. Elsevier, pp 73–102
50. Petrat T, Brunner-Schwer C, Graf B et al (2019) Microstructure of Inconel 718 parts with constant mass energy input manufactured with direct energy deposition. *Procedia Manuf* 36:256–266
51. Bax B, Rajput R, Kellet R et al (2018) Systematic evaluation of process parameter maps for laser cladding and directed energy deposition. *Addit Manuf* 21:487–494
52. Terrassa KL, Smith TR, Jiang S et al (2019) Improving build quality in directed energy deposition by cross-hatching. *Mater Sci Eng A* 765:138269. <https://doi.org/10.1016/j.msea.2019.138269>
53. MAZAK (2020) Additive manufacturing: the integration of additive manufacturing technology and multi-tasking machining. <https://www.mazakeu.co.uk/AM/>. Accessed 08 Apr 2020
54. Trumpf (2020) Laser metal deposition (LMD). [https://www.trumpf.com/en\\_GB/applications/additive-manufacturing/laser-metal-deposition-lmd/](https://www.trumpf.com/en_GB/applications/additive-manufacturing/laser-metal-deposition-lmd/). Accessed Mar 17, 2020
55. Azarniya A et al (2019) Additive manufacturing of Ti-6Al-4V parts through laser metal deposition (LMD): process, microstructure, and mechanical properties. *J Alloys Compd* 804:163–191
56. Jinoop AN, Paul CP, Mishra SK et al (2019) Laser additive manufacturing using directed energy deposition of Inconel-718 wall structures with tailored characteristics. *Vacuum* 166:270–278
57. Liu DR, Wang SH, Yan WT (2020) Grain structure evolution in transition-mode melting in direct energy deposition. *Mater Des* 194:108919. <https://doi.org/10.1016/j.matdes.2020.108919>
58. Dinovitzer M, Chen X, Laliberte J et al (2018) Effect of wire and arc additive manufacturing (WAAM) process parameters on bead geometry and microstructure. *Addit Manuf* 26:138–146
59. Wu BT, Pan ZX, Ding DH et al (2018) A review of the wire arc additive manufacturing of metals: properties, defects and quality improvement. *J Manuf Process* 35:127–139
60. McAndrew AR, Rosales MA, Colegrove PA et al (2018) Interpass rolling of Ti-6Al-4V wire + arc additively manufactured features for microstructural refinement. *Addit Manuf* 21:340–349
61. Tabernero I, Paskual A, Álvarez P et al (2018) Study on arc welding processes for high deposition rate additive manufacturing. *Procedia CIRP* 68:358–362
62. Li JZ, Alkahari MR, Rosli NA et al (2019) Review of wire arc additive manufacturing for 3D metal printing. *Int J Autom Technol* 13(3):346–353
63. Ding D, Pan Z, Cuiuri D et al (2015) Wire-feed additive manufacturing of metal components: technologies, developments and future interests. *Int J Adv Manuf Technol* 81(1/4):465–481

64. Prado-Cerqueira JL, Diéguez JL, Camacho AM (2017) Preliminary development of a wire and arc additive manufacturing system (WAAM). *Procedia Manuf* 13:895–902
65. Zhang X, Cui W, Li W et al (2019) A hybrid process integrating reverse engineering, pre-repair processing, additive manufacturing, and material testing for component remanufacturing. *Materials* 12(12):1961. <https://doi.org/10.3390/ma12121961>
66. Schmidt J (2020) Stable honeycomb structures and temperature based trajectory optimization for wire-arc additive manufacturing georg radow. *Optim Eng* 22:913–974
67. Ziaee M, Crane NB (2019) Binder jetting: a review of process, materials, and methods. *Addit Manuf* 28:781–801
68. Bai Y, Williams CB (2018) Binder jetting additive manufacturing with a particle-free metal ink as a binder precursor. *Mater Des* 147:146–156
69. Lv X, Ye F, Cheng L et al (2019) Binder jetting of ceramics: powders, binders, printing parameters, equipment, and post-treatment. *Ceram Int* 45(10):12609–12624
70. Binder Jetting (BJ) (2020) Additive manufacturing. <http://additivemanufacturing.com/tag/binder-jetting/>. Accessed 11 May 2020
71. Vangapally S, Agarwal K, Sheldon A et al (2017) Effect of lattice design and process parameters on dimensional and mechanical properties of binder jet additively manufactured stainless steel 316 for bone scaffolds. *Procedia Manuf* 10:750–759
72. Digital metal (2020) Components. <https://digitalmetal.tech/>. Accessed 11 May 2020
73. Cramer CL, Nandwana P, Yan J et al (2019) Binder jet additive manufacturing method to fabricate near net shape crack-free highly dense Fe-6.5 wt.% Si soft magnets. *Heliyon* 5(11):e02804. <https://doi.org/10.1016/j.heliyon.2019.e02804>
74. AZO materials (2012) Tool steel classifications. <https://www.azom.com/article.aspx?ArticleID=6138>. Accessed 11 May 2020
75. Alizadeh E (2008) Factors influencing the machinability of sintered steels. *Powder Metall Met Ceram* 47(5/6):304–315
76. Grzesik W (2017) Machinability of engineering materials. In Grzesik W (ed) *Advanced machining processes of metallic materials*, 2nd edn. Elsevier, Amsterdam, pp 241–264
77. Jin LZ, Sandström R (1994) Machinability data applied to materials selection. *Mater Des* 15(6):339–346
78. O'Sullivan D, Cotterell M (2002) Machinability of austenitic stainless steel SS303. *J Mater Process Technol* 124(1/2):153–159
79. Lanz RW, Melkote SN, Kotnis MA (2002) Machinability of rapid tooling composite board. *J Mater Process Technol* 127(2):242–245
80. Thakur DG, Ramamoorthy B, Vijayaraghavan L (2009) Study on the machinability characteristics of superalloy Inconel 718 during high speed turning. *Mater Des* 30(5):1718–1725
81. Benghersallah M, Boulanour L, Coz GL et al (2010) Machinability of Stellite 6 hardfacing. *EPJ Web of Conferences* 6:02001. <https://doi.org/10.1051/epjconf/20100602001>
82. Hasan MS, Mazid AM, Clegg R (2016) The basics of Stellites in machining perspective. *Int J Eng Mater Manuf* 1(2):35–50
83. Sandberg N (2012) On the machinability of high performance tool steels. *Digit Compr Summ Uppsala Diss from Fac Sci Technol* 927:400
84. Zhang PR, Liu ZQ, Guo YB (2017) Machinability for dry turning of laser clad parts with conventional vs. wiper insert. *J Manuf Process* 28:494–499
85. Courbon C et al (2019) Near surface transformations of stainless steel cold spray and laser cladding deposits after turning and ball-burnishing. *Surf Coatings Technol* 371:235–244
86. Wang C, Li K, Chen M et al (2015) Evaluation of minimum quantity lubrication effects by cutting force signals in face milling of Inconel 182 overlays. *J Clean Prod* 108:145–157
87. Lee JC, Kang HJ, Chu WS et al (2007) Repair of damaged mold surface by cold-spray method. *CIRP Ann Manuf Technol* 56(1):577–580
88. Jhavar S, Paul CP, Jain NK (2013) Causes of failure and repairing options for dies and molds: a review. *Eng Fail Anal* 34:519–535
89. Silva B, Pires I, Quintino L (2008) Welding technologies for repairing plastic injection moulds. *Mater Sci Forum* 587/588:936–940
90. Ahn DG, Lee HJ, Cho JR et al (2016) Improvement of the wear resistance of hot forging dies using a locally selective deposition technology with transition layers. *CIRP Ann Manuf Technol* 65(1):257–260
91. Cora ÖN, Koç M (2018) Wear resistance evaluation of hard-coatings for sheet blanking die. *Procedia Manuf* 15:590–596
92. Ratna D (2012) Thermal properties of thermosets. In: Guo Q (ed) *thermosets*, Woodhead Publishing, Cambridge, UK, pp 62–91
93. Valls I, Hamasaiid A, PadréA (2017) High thermal conductivity and high wear resistance tool steels for cost-effective hot stamping tools. In: *The 36th IDDRG conference-materials modelling and testing for sheet metal forming*, Munich, Germany
94. Launey ME, Ritchie RO (2009) On the fracture toughness of advanced materials. *Adv Mater* 21(20):2103–2110
95. Viale D, Béguinot J, Chenou F (2002) Optimizing microstructure for high toughness cold-work tool steels. In: *Proceedings of the 6th international tooling conference-the use of tool steels*, Karlsbad, Sweden, pp 299–318
96. Cornacchia G, Gelfi M, Faccoli M et al (2008) Influence of aging on microstructure and toughness of die-casting die steels. *Int J Microstruct Mater Prop* 3(2/3):195–205
97. Ebara R (2010) Fatigue crack initiation and propagation behavior of forging die steels. *Int J Fatigue* 32(5):830–840
98. Lee YC, Chen FK (2001) Fatigue life of cold-forging dies with various values of hardness. *J Mater Process Technol* 113(1/3):539–543
99. Ebara R, Kubota K (2008) Failure analysis of hot forging dies for automotive components. *Eng Fail Anal* 15(7):881–893
100. Davis JR (1995) *ASM specialty handbook: tool materials*. ASM International, Ohio, USA
101. Wilson WRD (1978) Friction and lubrication in bulk metal-forming processes. *J Appl Metalwork* 1(1):7–19
102. Dacic Z (2013) Tribological principles and measures to reduce cutting tools wear. In: *International conference on mechanical technology and structural materials*, Split, Croatia
103. Wu G, Xu C, Xiao G et al (2015) Self-lubricating ceramic cutting tool material with the addition of nickel coated CaF<sub>2</sub> solid lubricant powders. *Int J Refract Met Hard Mater* 56:51–58
104. Torres H, Caykara T, Rojacz H et al (2019) The tribology of Ag/MoS<sub>2</sub>-based self-lubricating laser claddings for high temperature forming of aluminium alloys. *Wear* 442/443:203110. <https://doi.org/10.1016/j.wear.2019.203110>
105. Cutting Tool Coating Production (2019) PM production machining. <https://www.productionmachining.com/blog/post/cutting-tool-coating-production>. Accessed 11 May 2020
106. Bobzin K (2017) High-performance coatings for cutting tools. *CIRP J Manuf Sci Technol*. <https://doi.org/10.1016/j.cirpj.2016.11.004>
107. Telasang G, Majumdar JD, Padmanabham G et al (2014) Effect of laser parameters on microstructure and hardness of laser clad and tempered AISI H13 tool steel. *Surf Coatings Technol* 258:1108–1118

108. Qamar SZ (2015) Heat treatment and mechanical testing of AISI H11 steel. *Key Eng Mater* 656/657:434–439
109. Herzog D, Seyda V, Wycisk E et al (2016) Additive manufacturing of metals. *Acta Mater* 117:371–392
110. Gorsse S, Hutchinson C, Gouné M et al (2017) Additive manufacturing of metals: a brief review of the characteristic microstructures and properties of steels, Ti-6Al-4V and high-entropy alloys. *Sci Technol Adv Mater* 18(1):584–610
111. Monkova K, Zetkova I, Kučerová L et al (2019) Study of 3D printing direction and effects of heat treatment on mechanical properties of MS1 maraging steel. *Arch Appl Mech* 89(5):791–804
112. Jäggle EA, Sheng Z, Kürnsteiner P et al (2017) Comparison of maraging steel micro- and nanostructure produced conventionally and by laser additive manufacturing. *Materials* 10(1):8. <https://doi.org/10.3390/ma100100082017>
113. Tan C, Zhou K, Kuang M et al (2018) Microstructural characterization and properties of selective laser melted maraging steel with different build directions. *Sci Technol Adv Mater* 19(1):746–758
114. Bai Y, Yang Y, Wang D et al (2017) Influence mechanism of parameters process and mechanical properties evolution mechanism of maraging steel 300 by selective laser melting. *Mater Sci Eng A* 703:116–123
115. Becker TH, Dimitrov D (2016) The achievable mechanical properties of SLM produced maraging steel 300 components. *Rapid Prototyp J* 22(3):487–494
116. Kempen K, Yasa E, Thijs L et al (2011) Microstructure and mechanical properties of selective laser melted 18Ni-300 steel. *Phys Procedia* 12(1):255–263
117. Yasa E, Kempen K, Kruth JP et al (2010) Microstructure and mechanical properties of maragings steel 300 after selective laser melting. In: *The 21st Annu Int Solid Free Fabr Symp-An Addit Manuf Conf SFF 2010*, pp 383–396
118. Tan C, Zhou K, Ma W et al (2017) Microstructural evolution, nanoprecipitation behavior and mechanical properties of selective laser melted high-performance grade 300 maraging steel. *Mater Des* 134:23–34
119. Yasa E, Kempen K, Kruth JP (2010) Microstructure and mechanical properties of maraging steel 300 after selective laser melting. In: *The 21st annual international solid freeform fabrication symposium: an additive manufacturing conference*, 9–11 August, Austin
120. Tan C, Zhou K, Tong X et al (2016) Microstructure and mechanical properties of 18Ni-300 maraging steel fabricated by selective laser melting. In: *Proceedings of the 6th international conference on advanced design and manufacturing engineering*, Zhuhai, China, pp 404–410
121. Junker D, Hentschel O, Schmidt M et al (2015) Qualification of laser based additive production for manufacturing of forging tools. *MATEC Web of Conf* 21:08010. <https://doi.org/10.1051/mateconf/20152108010>
122. Cottam R, Wang J, Luzin V (2014) Characterization of microstructure and residual stress in a 3D H13 tool steel component produced by additive manufacturing. *J Mater Res* 29(17):1978–1986
123. Ackermann M, Šafka J, Voleský L et al (2018) Impact testing of H13 tool steel processed with use of selective laser melting technology. *Mater Sci Forum* 919:43–51
124. Narvan M, Al-Rubaie KS, Elbestawi M (2019) Process-structure-property relationships of AISI H13 tool steel processed with selective laser melting. *Materials* 12(14):1–20
125. Yan JJ, Zheng DL, Li HX (2017) Selective laser melting of H13: microstructure and residual stress. *J Mater Sci* 52(20):12476–12485
126. Mertens R, Vrancken B, Holmstock N et al (2016) Influence of powder bed preheating on microstructure and mechanical properties of H13 tool steel SLM parts. *Phys Procedia* 83:882–890
127. Åsberg M, Fredriksson G, Hatami S et al (2018) Influence of post treatment on microstructure, porosity and mechanical properties of additive manufactured H13 tool steel. *Mater Sci Eng A* 742:584–589
128. Mazumder J, Choi J, Nagarathnam K et al (1997) The direct metal deposition of H13 tool steel for 3-D components. *Jom* 49(5):55–60
129. Pinkerton AJ, Li L (2005) Direct additive laser manufacturing using gas- and water-atomised H13 tool steel powders. *Int J Adv Manuf Technol* 25(5/6):471–479
130. Xue L, Chen J, Wang SH (2013) Freeform laser consolidated H13 and CPM 9V tool steels. *Metallogr Microstruct Anal* 2(2):67–78
131. Park JS, Park JH, Lee MG et al (2016) Effect of energy input on the characteristic of AISI H13 and D2 tool steels deposited by a directed energy deposition process. *Metall Mater Trans A Phys Metall Mater Sci* 47(5):2529–2535
132. Wang T, Zhang Y, Wu Z et al (2018) Microstructure and properties of die steel fabricated by WAAM using H13 wire. *Vacuum* 149:185–189. <https://doi.org/10.1016/j.vacuum.2017.12.034>
133. Ge J, Ma T, Chen Y et al (2019) Wire-arc additive manufacturing H13 part: 3D pore distribution, microstructural evolution, and mechanical performances. *J Alloys Compd* 783:145–155
134. Moradi M, Meiabadi S, Kaplan A (2019) 3D printed parts with honeycomb internal pattern by fused deposition modelling; experimental characterization and production optimization. *Met Mater Int* 25(5):1312–1325
135. Yang Y, Gu D, Dai D et al (2018) Laser energy absorption behavior of powder particles using ray tracing method during selective laser melting additive manufacturing of aluminum alloy. *Mater Des* 143:12–19
136. Shamsaei N, Yadollahi A, Bian L et al (2015) An overview of direct laser deposition for additive manufacturing; Part II: mechanical behavior, process parameter optimization and control. *Addit Manuf* 8:12–35
137. Abioye TE, Farayibi PK, Clare AT (2017) A comparative study of Inconel 625 laser cladding by wire and powder feedstock. *Mater Manuf Process* 32(14):1653–1659
138. Abioye TE, McCartney DG, Clare AT (2015) Laser cladding of Inconel 625 wire for corrosion protection. *J Mater Process Technol* 217:232–240
139. Yao J, Ding Y, Liu R et al (2018) Wear and corrosion performance of laser-clad low-carbon high-molybdenum Stellite alloys. *Opt Laser Technol* 107:32–45
140. Abioye TE, Medrano-Tellez A, Farayibi PK et al (2017) Laser metal deposition of multi-track walls of 308LSi stainless steel. *Mater Manuf Process* 32(14):1660–1666
141. Turichin GA, Klimova-Korsmik O (2018) Theory and technology of direct laser deposition. In: Shishkovsky I (ed) *Additive manufacturing of high-performance metals and alloys-modeling and optimization*, IntechOpen Limited, London
142. Hutasoit N, Yan W, Cottam R et al (2013) Evaluation of microstructure and mechanical properties at the interface region of laser-clad Stellite 6 on steel using nanoindentation. *Metallogr Microstruct Anal* 2(5):328–336
143. Moradi M, Ashoori A, Hasani A (2020) Additive manufacturing of stellite 6 superalloy by direct laser metal deposition—Part I: Effects of laser power and focal plane position. *Opt Laser Technol* 131:106328. <https://doi.org/10.1016/j.optlastec.2020.106328>

144. Foster J, Cullen C, Fitzpatrick S et al (2019) Remanufacture of hot forging tools and dies using laser metal deposition with powder and a hard-facing alloy Stellite 21<sup>®</sup>. *J Remanufacturing* 9(3):189–203
145. Davis JR (2000) Nickel, cobalt, and their alloys. ASM International, Geauga, US
146. Ding Y, Liu R, Yao J et al (2017) Stellite alloy mixture hard-facing via laser cladding for control valve seat sealing surfaces. *Surf Coatings Technol* 329:97–108
147. Ganesh P, Moitra A, Tiwari P et al (2010) Fracture behavior of laser-clad joint of Stellite 21 on AISI 316L stainless steel. *Mater Sci Eng A* 527(16/17):3748–3756
148. Wang D, Zhao H, Wang H et al (2017) Failure mechanism of a Stellite coating on heat-resistant steel. *Metall Mater Trans A Phys Metall Mater Sci* 48(9):4356–4364
149. Brownlie F, Hodgkiess T, Pearson A et al (2017) Effect of nitriding on the corrosive wear performance of a single and double layer Stellite 6 weld cladding. *Wear* 376/377:1279–1285
150. Kitamura Y, Morisada Y, Fujii H et al (2017) Effect of friction stir processing on microstructure of laser clad cobalt-based alloy. *Weld Int* 31(4):278–283
151. Sun S, Durandet Y, Brandt M (2005) Parametric investigation of pulsed Nd: YAG laser cladding of stellite 6 on stainless steel. *Surf Coatings Technol* 194(2/3):225–231
152. Singh R, Kumar D, Mishra SK et al (2014) Laser cladding of Stellite 6 on stainless steel to enhance solid particle erosion and cavitation resistance. *Surf Coatings Technol* 251:87–97
153. Díaz E, Amado JM, Montero J et al (2012) Comparative study of Co-based alloys in repairing low Cr-Mo steel components by laser cladding. *Phys Procedia* 39:368–375
154. Traxel KD, Bandyopadhyay A (2018) First demonstration of additive manufacturing of cutting tools using directed energy deposition system: Stellite<sup>TM</sup>-based cutting tools. *Addit Manuf* 25:460–468
155. Ren B, Zhang M, Chen C et al (2017) Effect of heat treatment on microstructure and mechanical properties of Stellite 12 fabricated by laser additive manufacturing. *J Mater Eng Perform* 26(11):5404–5413
156. Muller P, Mognol P, Hascoet JY (2013) Modeling and control of a direct laser powder deposition process for functionally graded materials (FGM) parts manufacturing. *J Mater Process Technol* 213(5):685–692
157. Yang Y, Zhang C, Wang D et al (2020) Additive manufacturing of WC-Co hardmetals: a review. *Int J Adv Manuf Technol* 108:1653–1673
158. Fortunato A, Valli G, Liverani E et al (2019) Additive manufacturing of WC-Co cutting tools for gear production. *Lasers Manuf Mater Process* 6(3):247–262
159. Chen J, Huang M, Fang ZZ et al (2019) Microstructure analysis of high density WC-Co composite prepared by one step selective laser melting. *Int J Refract Met Hard Mater* 84:104980. <https://doi.org/10.1016/j.ijrmhm.2019.104980>
160. Domashenkov A, Borbély A, Smurov I (2017) Structural modifications of WC/Co nanophased and conventional powders processed by selective laser melting. *Mater Manuf Process* 32(1):93–100
161. Uhlmann E, Bergmann A, Gridin W (2015) Investigation on additive manufacturing of tungsten carbide-cobalt by selective laser melting. *Procedia CIRP* 35:8–15
162. Ku N, Pittari JJ, Kilczewski S et al (2019) Additive manufacturing of cemented tungsten carbide with a cobalt-free alloy binder by selective laser melting for high-hardness applications. *Addit Manuf Compos Complex Mater* 71:1535–1542
163. Khmyrov RS, Safronov VA, Gusarov AV (2016) Obtaining crack-free WC-Co alloys by selective laser melting. *Phys Procedia* 83:874–881
164. Li CW, Chang KC, Yeh AC (2019) On the microstructure and properties of an advanced cemented carbide system processed by selective laser melting. *J Alloys Compd* 782:440–450
165. Gu D (2015) Laser additive manufacturing of high-performance materials. Springer, Berlin Heidelberg
166. Campanelli SL, Contuzzi N, Posa P et al (2019) Printability and microstructure of selective laser melting of WC/Co/Cr powder. *Materials* 12(15):2397. <https://doi.org/10.3390/ma12152397>